Engineered 3D Immuno-Glial-Neurovascular Human Brain Model

Alice E. Stanton[1†], Adele Bubnys[2,3†], Emre Agbas[2,3], Benjamin James[4], Dong Shin Park[2,3], Alan Jiang[2,3], Rebecca L. Pinals[2,3], Nhat Truong[2,3], Anjanet Loon[2,3], Colin Staab[2,3], Liwang Liu[2,3], Oyku Cerit[2,3], Hsin-Lan Wen[2,3], Manolis Kellis[3,5,7], Joel W. Blanchard[2,3,10*], Robert S. Langer[1,6,7,8,9*], Li-Huei Tsai[2,3,5*].

[1]Koch Institute, Massachusetts Institute of Technology; Cambridge, USA.

[2]Picower Institute for Learning and Memory, Massachusetts Institute of Technology; Cambridge, USA.

[3]Department of Brain and Cognitive Sciences, Massachusetts Institute of Technology; Cambridge, USA.

[4]Department of Electrical Engineering and Computer Science, Massachusetts Institute of Technology; Cambridge, USA.

[5]Broad Institute of Harvard and Massachusetts Institute of Technology; Cambridge, USA.

[6]Department of Chemical Engineering, Massachusetts Institute of Technology; Cambridge, USA.

[7]Department of Anesthesiology, Boston Children's Hospital; Cambridge, USA.

[8]Division of Health Science and Technology, Massachusetts Institute of Technology; Cambridge, USA.

[9]Institute for Medical Engineering and Science, Massachusetts Institute of Technology. Cambridge, USA.

[10]Current address: Department of Neuroscience, Black Family Stem Cell Institute, Ronald M. Loeb Center for Alzheimer's Disease, Icahn School of Medicine at Mt. Sinai, New York, NY 10029

*Co-corresponding authors. Email: lhtsai@mit.edu, rlanger@mit.edu, joel.blanchard@mssm.edu

†These authors contributed equally to this work.

Abstract: Patient-specific, human-based cellular models that integrate biomimetic BBB, immune, and myelinated neuron components are critically needed to enable translationally relevant and accelerated discovery of neurological disease mechanisms and interventions. By engineering a brain-mimicking 3D hydrogel and co-culturing all six major brain cell types derived from patient iPSCs, we have constructed, characterized, and utilized a multicellular integrated brain (miBrain) immuno-glial-neurovascular model with *in vivo*-like hallmarks. As proof of principle, here we utilized the miBrain to model Alzheimer's Disease pathologies associated with *APOE4* genetic risk. *APOE4* miBrains differentially exhibit amyloid

aggregation, tau phosphorylation, and astrocytic GFAP. Unlike the co-emergent fate specification of glia and neurons in organoids, miBrains integrate independently differentiated cell types in a modular system with unique utility for elucidating cell-type specific contributions to pathogenesis. We here harness this feature to identify that risk factor *APOE4* in astrocytes promotes tau pathogenesis and neuronal dysregulation through crosstalk with microglia.

One-Sentence Summary: A novel patient-specific brain model with BBB, neuronal, immune, and glial components was developed, characterized, and harnessed to model Alzheimer's Disease-associated pathologies and *APOE4* genetic risk.

In vitro brain models hold enormous potential for decoding disease mechanisms and establishing enhanced drug screening platforms with which increasingly translatable therapeutics can be discovered and developed (*1–6*). As genetic differences limit the pace and fidelity of therapeutic translation from rodent models to human (*7*), human cell-based models offer an attractive alternative. Neurological diseases have been particularly hindered by the lack of human-based models, as many genetic risk variants lie in non-coding regions and there are marked differences between the human brain and that of other species (*8*). Furthermore, the time-intensiveness of generating animal models for targeted disease mutations is a bottleneck for the study of many diseases and variants (*8*) and the lack of model systems with which to assess phenotype correction precludes effective therapeutic development (*9*). Induced pluripotent stem cell (iPSC) technology, in which human patient cells from a simple biopsy can be reprogrammed and differentiated into almost any cell type in the body (*10*, *11*), enables the generation of human patient-specific cells. More recently, brain organoids, harnessing iPSCs, have enhanced neuronal maturation beyond that attainable in neuronal monoculture and provided a model of neuronal development with an emergent approach whereby neuronal progenitors differentiate together into a dense co-culture of neurons and glia with a maintained progenitor population with diverse signatures (*1–3*, *12*). At the same time, others, including our laboratory, have taken more directed approaches to construct microphysiological systems with tissue-mimicking 3D architecture in which human primary cells or human iPSC-derived cells of the desired lineages are combined in a 3D scaffold, forming a specific architecture via cell self-assembly or via patterning (*4*, *5*, *13–17*). Following this approach, our laboratory has recently established a fully iPSC-based 3D triculture model of the blood-brain barrier (BBB) and demonstrated the utility of such patient-specific models for elucidating mechanisms of genetic risk (*18*).

Given the key role of glial, immune, and vascular cells in healthy brain physiological processes and that non-cell autonomous effects contribute critically to neurodegenerative disease (*19–23*), there is great interest in establishing vascularized brain models with all relevant CNS cell types and biomimetic tissue architecture. Further, to identify cell type- and pathway-specific contributions to pathogenesis, it would be advantageous to construct a brain model in which each cell type could be independently modified. To realize these possibilities, we have developed a 3D, iPSC-based multicellular integrated brain (miBrain) immuno-glial-neurovascular model. As conventional 3D microphysiological systems utilize protein-based materials that only mimic the basement membrane, such as Matrigel and collagen, or rely on fibrin like which forms during blood clots and which contains neurotoxic components (*24*), all of which are rapidly degrading, we critically needed a hydrogel mimetic of brain tissue beyond the basement membrane and which could promote neuronal activity, while providing 3D structure and supporting cellular self-assembly. To this end, we engineered a novel 3D hydrogel, Neuromatrix, to provide enhanced

brain mimicry and promote co-self-assembly of endothelial cells, pericytes, astrocytes, oligodendroglia, microglia, and neurons into an integral engineered tissue. As proof of principle, we have leveraged the miBrain to investigate the strongest genetic risk factor for sporadic Alzheimer's Disease (AD), apolipoprotein E4 *(APOE4)* (*25*). Importantly, we have modeled amyloid and tau pathologies in this integrated brain model and uncovered that *APOE4* astrocytes are sufficient to induce reactive species and tau phosphorylation via crosstalk with microglia.

3D Immuno-Glial-Neurovascular miBrain Model

Human neurological disease often involves a diversity of cell types beyond neurons but there are currently no models that have both this full cellular diversity and human genetics (*26*). Accordingly, there is great interest in vascularizing brain organoids or integrating neurons and other CNS cell types into microphysiological systems. We endeavored to address this critical void with an approach that can recapitulate brain-mimetic 3D architecture and also decouple glial and neuronal fate specification, enabling cell type-specific perturbations and genetic mutations for mechanistic inquiry and targeted therapeutic development. To this end, we separately differentiated each of the six major brain cell types from patient-specific iPSCs optimized from published protocols and validated via immunoreactivity of canonical markers and flow cytometry-based analysis for brain microvascular endothelial cells (BMECs) (*27*) (**Fig. S1A,G**), pericytes (*27, 28*) (**Fig. S1B,H**), oligodendrocyte precursor cells (OPCs) (*29*) (**Fig. S1C,J**), neurons (*30*) (**Fig. S1D,K**), astrocytes (*31*) (**Fig. S1E,I**), and microglia-like cells (iMG)(*32*) (**Fig. S1F,L**). Upon validated fate specification for each lineage, cells are combined into a novel 3D hydrogel we engineered to mimic key aspects of brain tissue, enabling cell co-culture and 3D network co-assembly and enhanced functional phenotypes, and seeded in 48-well plates for high throughput formation of integral 3D tissue we refer to as the multicellular integrated brain (miBrain) (**Fig. 1A**). All cells are co-encapsulated on day 0 with the exception of iMG, which are added to the co-culture on day 7 and migrate into the engineered tissue. Together the cells spread and form 3D networks by day 5 and mature into an integral tissue mimic until the conclusion of desired assays. miBrains are characterized by their composition, including all six major CNS cell types together, and their emergent 3D morphologies and brain-like functionalities. They form 3D neurovascular units of mature, myelinated neurons, inclusive of a BBB with BMECs, pericytes, and astrocytes, and resident-immune cells of the brain, microglia (**Fig. 1B**). As in the human brain, in the miBrain pericytes home to the microvasculature, tightly associating with the BMEC networks that express tight junctions, and astrocytes spread and exhibit star-like morphologies, expressing GFAP and transporter AQP4 at the BBB. Neurons extend projections in close proximity to vessel networks, are ensheathed by myelin produced by oligodendrocytes, and interact with microglia (**Fig. 1B**).

Engineering Brain Matrix-Inspired 3D Hydrogel

Given that current *in vitro* models typically co-culture a maximum of three different cell types stably, to enable the co-culture of all six major CNS cell types into an integral 3D tissue we looked to the human brain for inspiration. The brain extracellular matrix (ECM) is predominantly comprised of a web of glycosaminoglycans and proteoglycans, enmeshing neuronal and glial cell types. Within this interstitial tissue reside vascular networks ensheathed in a very thin layer of basement membrane proteins (*33*). These ECM components provide both structural support and important biochemical signaling factors, and they are implicated in a plethora of physiological processes and pathological phenotypes (*33, 34*).

We hypothesized that brain-matrix proteins that are normally expressed in the brain at later stages of development could be harnessed to accelerate maturation. We reasoned that if we could mimic brain tissue by constructing a soft 3D hydrogel with brain-mimetic components, we could provide scaffolding to encapsulated cells at the same time as promoting enhanced brain cell phenotypes. To rapidly begin to assay differential effects of brain-matrix components we encapsulated combinations of hyaluronic acid, heparin, reelin, tenascin-R (TenR), tenascin-C (TenC), brevican (BCN), versican (VCN), neurocan (NCN), and thrombospondin-1 (TSP1) in Matrigel with BMECs, pericytes, astrocytes, oligodendrocytes, and neurons (**Fig. S2A**). The number of neuronal projections and presence of myelin basic protein (MBP) was low overall across these Matrigel-encapsulated conditions, with a small number of neuronal projections in the VCN condition (**Fig. S2A,B**). In parallel, we assayed electrical activity in these cultures via a multi-electrode array (MEA). Electrical activity was low across these conditions and only occasional spikes of neurons firing were detected even after several weeks in culture, though VCN again promoted a slightly increased firing rate (**Fig. S2C,D**).

As Matrigel is a heterogeneous admixture of mouse tumor basement membrane proteins with limited mechanical and biochemical tunability (*35*) and rapidly degrading, as is common with protein-based biomaterials, we sought a more tunable and biochemically-defined scaffolding with which to present the brain-matrix cues. The brain is largely comprised of a web of hyaluronan glycosaminoglycan (GAG) chains enmeshing cells and other proteins, scaffolding perineuronal nets (*33*). Dextran is a GAG biochemically similar yet distinct from hyaluronan, providing a uniquely biosimilar scaffold compared to other synthetic polymers such as polyethylene glycol (PEG), while still presenting a bioorthogonal backbone that can be mechanically tuned independently from brain-specific biochemical cues (*36*). Dextran hydrogels can be fabricated at soft stiffnesses and with viscoelastic properties akin to that of brain tissue (*37*). We screened dextran-based hydrogels in conjunction with PEG hydrogels, a biochemically inert polymer that has similar advantages with respect to tunability; glycosil, a hyaluronan-based hydrogel; and heprasil, a hydrogel with hyaluronan and heparin. Encapsulating miBrain cells in each of these hydrogels in conjunction with crosslinker and basement membrane peptide mimic, RGD, led to the establishment of a 3D co-culture inclusive of neuronal projections (**Fig. S2E,F**). Vascular networks were also observed in the dextran-based hydrogel conditions, while only small regions positive for BMEC marker PECAM were observed in other conditions (**Fig. S2E,F**). Further, on the MEA, miBrains encapsulated in PEG-, heprasil-, and glycosil-based hydrogels displayed only low levels of electrical activity (**Fig. S2G**). In light of these results, we decided to further screen dextran-based hydrogels, screening across mechanical compositions that could support integrated neurovascular unit formation in miBrains. We cultured miBrains in hydrogels across mechanical stiffness conditions by altering the molar amounts of dextran macromer and non-degradable peptide crosslinker reacted, wherein intermediate molar ratios yielded the most robust vessel networks and neuronal projections, evaluated in terms of vessel segment area and neuronal marker intensity (**Fig. S2H,I**). For this optimal stiffness condition, we modulated degradability by introducing a PEG non-degradable crosslinker at various concentrations. Both the 100% degradable and 90% degradable hydrogel promoted neurovascular unit assembly, with integrated microvascular networks and neuronal projections (**Fig. S2J,K**). We found both formulations to be suitable for supporting miBrain phenotypes for our experiments and chose to utilize the 100% degradable condition to simplify the technical scale up of miBrain formation.

Now with a brain-mimicking hydrogel scaffold in place to support miBrain co-culture, we revisited

the hypothesis that brain matrix-specific proteins incorporated into a hydrogel, structurally capable of supporting their conjugation and presentation to cells, could be used to promote neuronal maturation. Screening across hydrogels incorporating HA, Heparin, Reelin, TenR, TenC, NCN, BCN, VCN, or TSP1, we co-cultured neurons and astrocytes and monitored neuronal activity on an MEA. After 2 weeks of culture, robust neuronal projections were observed across the hydrogel conditions, particularly in hydrogels incorporated with VCN, HA, TenC, and TSP1 (**Fig. S3A,B**). Strikingly, many of these matrix component conditions led to robust neuronal spiking on MEA recordings by week 2 in culture, a very short onset time for iPSC-derived neurons. Representative raster plots of conditions demonstrate spiking across electrodes and bursts (**Fig. S3C**). Of the conditions tested, VCN, Reelin, BCN, TenC, NCN, and TSP1 displayed the highest firing rates (**Fig. S3D**). Given these promising results, we selected a subset of these ECM proteins that also supported hydrogel mechanical integrity and integrated these various brain-matrix proteins into our engineered dextran-based hydrogel with all miBrain cell types. Robust cultures and neuronal projections formed throughout the co-culture in many conditions, particularly for VCN (**Fig. 1C**). In terms of immunoreactivity of neuronal marker neurofilament, VCN and BCN led to the strongest signal intensity (**Fig. 1D**). Assessing these conditions on the MEA system in parallel, VCN and heparin displayed the highest neuronal firing rate (**Fig. 1E**). Across the many assays and experimental replicates tested we found VCN to be a consistent top-performer. Our engineered dextran-based hydrogel incorporating VCN protein led to a reproducibly robust hydrogel scaffolding for the miBrain. While neurovascular units in miBrains suffered from the breakdown of Matrigel over time, robust neurovascular phenotypes persisted in our dextran-based hydrogel through the initial testing time of 5 weeks (**Fig. 1F**) and with enhanced structural integrity (**Fig. 1G**) and neuronal activity (**Fig. 1H**) compared to Matrigel. We therefore chose VCN-integrated dextran-based engineered hydrogels at the optimized polymer ratios for miBrain formation, terming the formulation "Neuromatrix."

Multicellular Integrated miBrain Platform Co-Assembling 6 Major CNS Cell Types

To establish this novel miBrain platform as a tool that could be widely deployed to decode CNS disease mechanisms and accelerate drug discovery and development, we sought to characterize each cell type and evaluate important biomimetic features. Given the utility of real-time monitoring for assessment of cellular dynamics, we simultaneously sought to integrate a multiplexed panel of biosensors for readouts of biological function in the miBrain platform. To monitor astrocytes in the miBrain in real-time, we fluorescently labeled astrocytes via AAV transfection prior to miBrain incorporation and introduced a fluorescent tubulin marker to label the neurons in live cultures. Astrocytes were observed to closely interact with neurons and extend dynamically motile processes (**Fig. 1I**). Given the important role of microglia in a variety of processes, including immune surveillance, blood-brain barrier function (*38*), and neuronal activity modulation and synaptic pruning (*39*, *40*), we sought to monitor microglia dynamics in the miBrain in real-time. We pre-labeled iMG and incorporated them into miBrains with BMECs differentiated from an mCherry-expressing iPSC line and treated with a fluorescent tubulin marker to label neurons. We observed motile iMG migrating through the miBrain and interacting with microvasculature (**Fig. 1J**). iMG closely associated with neuronal projections were highly dynamic, extending fast-moving processes (**Fig. 1Ki**) and physically moving neuronal projections (**Fig. 1Kii**). The tools we adopted for live imaging cellular interactions and dynamics could be harnessed to probe many combinations of cell types, beneficial for a wide variety of biological questions and applications.

Characterization of Blood-Brain Barrier Integrated in miBrain

An ideal brain model would contain an integrated, 3D BBB expressing the physiologically-relevant transporters and receptors present in the human BBB, surrounded by the diversity of cell types that play key roles in reinforcing the barrier and contributing to disease pathogenesis. We sought to probe BBB phenotypes in the miBrain evaluating canonical markers for validation of human-BBB hallmarks, as well as transcriptomic analyses, to widely profile gene expression of BBB cell types within the brain-mimetic miBrain niche. BMECs form networks fully integrated into the miBrain and extending throughout the engineered tissue mimic (**Fig. 2A**). These microvascular networks express adhesion proteins VE-CAD (**Fig. 2B**) and PECAM (**Fig. 2C**) and tight junction markers ZO-1 and CLDN-5 (**Fig. 2C**).

Interacting with the brain microvasculature and forming the parenchymal niche of the BBB are astrocytes. These important glial cells, while also performing essential roles in neuronal regulation, have regulatory roles in vascular and barrier function (*41*). iPSC-derived astrocytes, however, often have limited maturity with low expression levels of canonical fate markers. In the miBrain, astrocytes express canonical marker GFAP and water channel AQP4 and extend endfeet onto the vasculature (**Fig. 1B**). At the BBB astrocytes express gap junctions comprised of connexins, including connexin-43 (Cx43). Validating additional key astrocyte markers we performed immunohistochemistry in miBrains for Cx43, observing positive immunoreactivity around the microvasculature (**Fig. 2D**), and canonical marker S100β (**Fig. 2E**). Given the limited maturity of iPSC-derived astrocytes conventionally, we sought to characterize miBrain-astrocytes and better understand the effect of this engineered brain niche on astrocyte signatures. We performed RNAseq on astrocytes isolated from miBrains and on monocultured astrocytes in samples processed in parallel (**Fig. S4A-C**). In the miBrain, astrocytes display a striking enrichment of identity genes like *S100β, SLC1A2,* and *ALDH1L1* (**Fig. 2F**). These astrocytes strongly upregulated a wide variety of genes involved in synaptic modulation and neuronal signaling (**Fig. S4D**) as well as vascular regulation (**Fig. S4E**), evidencing the recapitulation of both barrier (including via *ROBO2* and *SEMA6A*) and neuronal process regulation (including via *NRP1*) in miBrain-astrocytes, among other differentially expressed genes (**Fig. S4F,G**). Consonantly, gene ontology analysis revealed a strong upregulation in biological pathways associated with neuronal processes and endothelial cell proliferation, as well as in extracellular matrix assembly (**Fig. 2G**). These data point to interactions between astrocytes and the other cell types comprising the miBrain niche and demonstrate how the miBrain niche can enhance iPSC-derived astrocyte signatures.

While endothelial cells are the primary regulators of BBB permeability and selectivity, pericytes in the human brain are coupled to capillaries and exercise key functions in BBB maintenance, transport regulation, and cerebrovascular blood flow (*42*). Correspondingly, in the miBrain pericytes localize to the outer lumen of the BMEC networks (**Fig. 2H**). As pericyte calcium increases in response to voltage-gated calcium channels and promotes contraction (*42*), we sought to assess their functional coupling to the microvasculature. We constructed miBrains with pericytes stably expressing GCaMP6 calcium indicator and monitored their calcium transients in miBrains (**Fig. 2I,J**). We stimulated vessels with potent vasoconstrictor endothelin-1 (ET-1), known to induce a prolonged increase in blood pressure *in vivo*, and monitored pericyte calcium signaling as a proxy for pericyte contractile activity. ET-1 stimulation induced network-wide pericyte calcium transients and this elevated calcium activity persisted for minutes (**Fig. 2K,L**),

indicating a robust pericyte response to vasomodulation.

Together, these data indicate the miBrain contains an integrated BBB with brain-like signatures, integrated into the surrounding neuronal networks and additional cell types of the brain niche.

Characterization of Neuronal Phenotypes in miBrain

Microglia and oligodendrocytes regulate multiple processes in the brain, with key roles in neuronal health and function, while also contributing to vascular regulation and other physiological functions (*43*, *44*). Given the sensitivity of microglia to environmental cues and the difficulty in maintaining homeostatic signatures of iPSC-derived microglia in *in vitro* systems, we wondered whether the brain-like niche of the miBrain would be conductive to *in vivo*-like microglia signatures. Through immunohistochemistry analysis, we observed that iMG incorporated into the miBrain integrate and extend processes in close association with the neurons and vasculature (**Fig. 3A**). miBrain-iMG display immunoreactivity to purinergic receptor P2RY12, involved in motility and associated with homeostatic processes (**Fig. 3A**). RNAseq analysis of iMG isolated from miBrains (**Fig. S5A,B**) revealed a large number of differentially expressed genes in miBrain-iMG compared to monocultured iMG processed in parallel (**Fig. S5C,D**). Importantly, key microglia identity genes are upregulated in the miBrain-iMG, including *CX3CR1*, *EGR1*, and *P2RY12* (**Fig. 3B, Fig. S5E**), the latter which we also validated through flow cytometry-based analysis on the protein level (**Fig. S5F**). Further, miBrain-iMG upregulated genes associated with neuronal signaling and endothelial cell processes (**Fig. 3C**). These results indicate that the miBrain niche promotes enhanced microglia signatures and provides a system in which their multi-faceted interactions with vascular and neuronal components can be further probed in high-resolution and high throughput.

Oligodendrocytes *in vivo* are the myelinating brain cell type and engage with neurons. Assessing oligodendroglia phenotypes in the miBrain, we detected positive myelin basic protein immunoreactivity (**Fig. 3D**). Analyzing the transcriptional signatures of oligodendroglia via RNAseq (**Fig. S6A-C**), miBrain-oligodendroglia display upregulation of genes associated with myelination (**Fig. 3E**). Among the genes upregulated in oligodendroglia in the miBrain (**Fig. S6D,E**), biological pathways associated with dendritic spine maintenance, neuron axon guidance, and myelination are significantly upregulated (**Fig. 3F**), including genes suggestive of neuronal interactions (such as *NDRG4*, *KIF1A*, and *SNAP25*; **Fig. S6F**) and of vascular interactions (such as *VEGFA*, *KDR*, *FLT4* and *NRP1*; **Fig. S6G**). Concomitantly, pathways associated with maintenance of neuronal stem cells (**Fig. 3F**) are strongly downregulated in miBrain-oligodendroglia while genes associated with maturation of OPCs are promoted (including *GPC1* and *PDGFRα*; **Fig. 3G**).

Harnessing doxycycline-inducible NGN2-iPSCs, neurons were differentiated and then cultured in the miBrain. Evaluating neuronal markers via immunohistochemistry, miBrain-neurons were found to be largely MAP2-positive (**Fig. 3H**) and express synaptic proteins, such as the presynaptic vGlut1 and postsynaptic PSD95 with a greater density than that of monocultured neurons (**Fig. 3I,J**). To assess neuronal activity in the miBrain we differentiated neurons from an iPSC line stably expressing tdTomato and GCaMP3. GCaMP-neurons integrated into miBrains form projections and display expected neuronal morphologies (**Fig. 3K**). Live monitoring calcium transients in GCaMP-neurons, spikes of neuronal activity were recorded over time (**Fig. 3L**) and miBrain cultures were compared to that of neuron monocultures across the neurons in each field of view

(**Fig. 3M**). Neurons in miBrains exhibited robust spikes of activity and displayed enhanced calcium transients compared to monocultured neurons (**Fig. 3N**). In parallel, we evaluated neuronal activity on the MEA system, culturing miBrains on the electrode array (**Fig. 3O**). Though miBrains are a 3D tissue and this method only captures activity on the bottom surface, we found that we were able to detect robust electrical activity (**Fig. 3P**). miBrains displayed enhanced spontaneous neuronal activity in terms of spike rate and burst rate (**Fig. 3Q**) and promoted stimulus responsiveness, decreasing the latency time to spiking upon electrical stimulation and increasing the subsequently evoked spikes (**Fig. 3R**). To evaluate the transcriptomic changes that neurons undergo in the miBrain, we virally labeled neurons with tdTomato and performed RNAseq on FACS isolated cells based on tdTomato expression (**Fig. S7A-C**). We observed a clear upregulation of neuronal genes (such as *SCN1A* and *CACNA1C;* **Fig. S7D**) and downregulation of genes associated with neuronal precursor cells (like *SOX11* and *PAX6;* **Fig. S7E**) in miBrain-neurons. While this viral transduction method could also be less cell type-specific than the non-viral methods we were able to harness for isolating other miBrain cell types, in that other cell types like iMG could potentially phagocytose labeled cell debris and contaminate the tdTomato-positive population, these neuronal signatures provide evidence of strong neuronal phenotypes in miBrain. Among the differentially expressed genes (**Fig. S7F,G**), genes associated with modulation of synaptic transmission, axon fasciculation, and astrocyte development are among those most strongly upregulated in miBrain-neurons. Conversely, neuronal stem cell population maintenance and neuroepithelial cell differentiation pathways are among those most strongly downregulated (**Fig. S7H**).

These results would suggest that the multicellular co-culture of the miBrain introduces not only important cell types that are often lacking in existing models, but that the key facets of physiological function they confer further promotes neuronal phenotypes. Given the amount of cellular crosstalk observed across transcriptomic analyses and the *in vivo*-like signatures induced in miBrain cells, this multicellular co-culture could provide substantial advantages for dissecting disease mechanisms and modeling neuropathologies.

Harnessing miBrain to Investigate Functional Consequences of *APOE4* Astrocytes

The *E4* allele of the gene encoding lipid transport protein apolipoprotein E (APOE) strongly increases risk for developing late-onset AD and decreases age of disease onset compared to the *E3* allele (*45*). Lipid accumulation in glia is a hallmark of AD (*46*) and in *APOE4* astrocytes, a major lipid and cholesterol-producing cell type in the brain (*47*), lipid metabolism pathways are perturbed (*48*), lipids accumulate (*49*, *50*), and cholesterol sequestration can promote brain matrisome changes (*51*). The functional consequences of *APOE4* astrocyte dysfunction on the other cell types in the brain niche and the question of if they contribute directly to AD-associated pathologies remain poorly understood. We therefore sought to investigate phenotypic changes in the multicellular miBrain niche with *APOE4* astrocytes.

While iPSC-derived astrocytes typically express only low levels of canonical astrocyte markers, we have found that the miBrain strongly promotes mature astrocyte signatures (**Fig. 1B; Fig. 2D-G; Fig. S4D,E**), as it does each of the other cell types profiled. Taking advantage of the resultant enhanced modeling capabilities, we constructed miBrains from isogenic sets of *APOE3/3* and *APOE4/4* iPSCs generated by CRIPSR-dCas9 editing (*48*). The *APOE3/3* cell line was derived from a cognitively normal individual and edited to *APOE4/4* homozygous, while an *APOE4/4* line from an AD patient was corrected to *APOE3/3*. We constructed miBrains using these lines and

evaluated GFAP signal, given the increasing utilization of GFAP as a biomarker for AD and its acceptance as an indicator of reactive astrocytes (*52*, *53*). We assessed GFAP immunoreactivity between *APOE3* and *APOE4* miBrains (**Fig. 4A**) and found that *APOE4* miBrains displayed increased GFAP intensity (**Fig. 4B**). Concomitantly, we evaluated marker S100β that defines a mature developmental stage in astrocytes (*54*) and reportedly drives a pro-inflammatory and neurodegenerative phenotype (*55*, *56*). Evaluating *APOE4* versus *APOE3* miBrains, higher S100β immunoreactivity was detected in the *APOE4* condition (**Fig. 4C,D**). As our laboratory's previous RNA-seq dataset on iPSC-derived *APOE4* versus *APOE3* astrocytes (*48*) indicates no significant difference in *GFAP* (**Fig. S8Ai**) nor *S100β* (**Fig. S8Aii**) gene expression, the differentially increased maturity and reactive phenotype in astrocytes of the *APOE4* miBrain is likely promoted by the miBrain, for example, via oxidative stress or related cell non-autonomous mechanisms.

To evaluate if these results mirror expression of astrocytes in human brains, we utilized a single-nucleus transcriptomic dataset our laboratory recently generated, characterizing post-mortem human brain samples from *APOE4/4*, *APOE3/4*, and *APOE3/3* individuals (*17*). We analyzed this data set for reactive astrocyte genes for *APOE4/4* and *APOE3/4* individuals versus *APOE3/3* individuals. We found a broadly increased expression of reactive astrocyte genes in *APOE4* carriers compared to non-carriers, including for *GFAP, S100β,* and *VIM* (**Fig. 4E**). Among the panel of reactive astrocyte genes evaluated, the most strongly upregulated were *LINGO1*, *HSPB1*, and *CRYAB* (**Fig. 4E**). We therefore sought to assess the functional consequences of the increased reactive phenotype of *APOE4* astrocytes.

While organoids cannot decouple astrocyte genotype from that of the other cell types due to their co-emergent differentiation from neuronal progenitors, the miBrain platform can uniquely decouple astrocyte genotype from that of the neurons and other cell types in the co-culture. Therefore, to assess astrocyte-specific contributions to *APOE4* pathogenesis we harnessed this advantageous miBrain capability to generate miBrains with *APOE3* neurons, iMG, oligodendroglia, pericytes, BMECs, and either *APOE3* or *APOE4* astrocytes.

Given that astrocytes play critical roles in regulating oxidative stress (*57*) and that reactive astrocytes can aggravate neuronal damage (*58*) and AD-associated pathological hallmarks, including via hydrogen peroxide production (*59*), we examined reactive species in the miBrain. Live assays for hydrogen peroxide, nitric oxide, and peroxynitrite were performed on miBrains with fluorescently labeled astrocytes, so that localization of reactive species in astrocytes versus in the surrounding cell types could be assessed. We detected higher levels of hydrogen peroxide colocalizing with astrocytes in the miBrains with *APOE4* astrocytes compared to the all-*APOE3* condition (**Fig. 4F,Gi**). Interestingly, increased hydrogen peroxide was also observed overall in the miBrains with *APOE4* astrocytes (**Fig. 4F, 4Gii**), including in neuron-colocalizing regions (**Fig. 4Giii**), determined using a live tubulin dye that strongly labels neurons (**Fig. 4Giii**). These results suggest that *APOE4* astrocytes harbor increased hydrogen peroxide and promote hydrogen peroxide in nearby cells, including in neurons.

In *APOE3* miBrains constructed with *APOE4* versus *APOE3* astrocytes, we also assessed nitric oxide using a live fluorescent indicator. Strikingly, bright intercellular droplets of nitric oxide were observed in miBrains with *APOE4* astrocytes (**Fig. 4H**). Between *APOE4*- versus *APOE3*-astrocyte miBrain conditions, more nitric oxide droplets were observed colocalizing with *APOE4* astrocytes (**Fig. 4H,Ii**) and in the overall for the *APOE4* astrocyte-containing miBrain, quantified in terms of total number and total area of nitric oxide droplets (**Fig. 4H,Iii,Iiii**). We similarly

evaluated *APOE3* miBrains with *APOE4* versus *APOE3* astrocytes with a live indicator for peroxynitrite (**Fig. S8Bi**). While no differences were detected in astrocyte-colocalizing peroxynitrite (**Fig. S8Bii**), a significant overall increase in peroxynitrite species (**Fig. S8Biii**) and neuron-colocalizing peroxynitrite (**Fig. S8Biv**), defined by tubulin-positive labeling, were detected. Together, these results provide evidence that not only do *APOE4* astrocytes harbor an increased proclivity to form hydrogen peroxide and nitric oxide species, but that they promote the accumulation of these species in neurons and other cells, which could contribute to *APOE4* neuropathologies.

Oxidative stress and free radicals, normally managed by lysosomal catabolism, can also, when imbalanced, contribute to lysosomal dysfunction, resulting in a vicious cycle that can exacerbate the cellular damage implicated in AD and other neurodegenerative diseases (*60*, *61*). We thus asked whether the *APOE4* astrocyte-induced changes in reactive species we observed are also associated with lysosomal changes. We returned to our single-nucleus transcriptomic dataset of *APOE4* carriers and non-carriers (*17*) to evaluate whether aberrant lysosomal processes were differentially expressed with *APOE4.* Differential gene expression was observed for regulation of lysosomal catabolism, with genes including *LRP1, LDLR,* and *ATP13A2* (**Fig. S8C**). Many related genes participate in regulation of oxidative stress-induced cell death, a pathway displaying upregulation of genes like *HSPB1, NFE2L2,* and *SOD1* and downregulation of *PRKN, PDE8A,* and *NME5* in astrocytes of *APOE4* carriers compared to non-carriers (**Fig. S8D**). To evaluate consequences of *APOE4* astrocytes on lysosomes in miBrains, we labeled lysosomes in *APOE3* miBrains constructed containing *APOE4* versus *APOE3* astrocytes (**Fig. S8E**). Interestingly, miBrains with *APOE4* astrocytes compared to all-*APOE3* miBrains displayed a clear increase in lysosomal particle area colocalizing with astrocytes (**Fig. S8Fi**) as well as in overall lysosomal particle area (**Fig. S8Fii**) and lysosomal intensity (**Fig. S8Fiii**) in the miBrain. These data suggest that *APOE4* astrocytes both harbor lysosomal dysfunction and promote it in other cells, with this dysfunction correlating with the concomitant increase in reactive species observed in miBrains with *APOE4* astrocytes (**Fig. 4F-I**).

miBrain Reveals *APOE4* Astrocyte Crosstalk with Microglia Promotes Neuronal Tau Phosphorylation.

Given that the miBrain can uniquely dissect cell type-specific contributions to pathology with the construction of miBrains from cells of all decoupled genotypes, including that of astrocytes, we here sought to test whether *APOE4* astrocytes contribute to the *APOE4*-associated proclivity to tau phosphorylation. *APOE4* has been shown to accelerate amyloid aggregation (*62*) and tau-mediated neurodegeneration (*63*), and evidence suggests that removal of astrocytic APOE4 is protective against tau pathology (*64*). Endogenously, *APOE4* miBrains display increased amyloid aggregation (**Fig. S9A,B**) and tau phosphorylation (**Fig. S9C-F**), here assessed at week 14 in culture, consistent with observations made by Lin et al., 2018 (*48*) using organoid culture. Notably, this includes the development of 4R tau pathology and at increased levels in *APOE4* compared to *APOE3* miBrains (**Fig. S9G,H**). To test whether *APOE4* astrocytes could promote tau phosphorylation, we compared *APOE3* miBrains with *APOE4* astrocytes to miBrains comprised of cells from all *APOE3* or *APOE4* backgrounds. To accelerate pathological progression, we cultured miBrains in the presence of a low 20 nM of exogenous amyloid beta peptide 1-42 (Aβ-42) resuspended at neutral pH. After 72 hours of treatment with Aβ-42, increased tau phosphorylation was observed in *APOE4* miBrains via immunoreactivity to phosphorylated tau antibody AT8, especially somatically (**Fig. 4J**). Interestingly, *APOE3* miBrains with *APOE4*

astrocytes also displayed substantial tau phosphorylation and increased somatic AT8 intensity compared to *APOE3* miBrains (**Fig. 4J,K**). These results suggest that *APOE4* astrocytes could have an important role in mediating tau pathological progression.

Canonical reactive A1 astrocytes are known to be induced through the secretion of cytokines by microglia (*65*) and microglia-astrocyte crosstalk is thought to mediate immune response to many neurological insult and disease conditions (*66*). We thus asked whether microglia signaling modulates the *APOE4* astrocyte-associated tau phosphorylation we observed. We cultured miBrains with and without iMG. Strikingly, in the absence of microglia, tau phosphorylation was substantially diminished in *APOE4* miBrains (**Fig. 4L,M**). While some aggregates displayed strong immunoreactivity to phosphorylated tau, inter-neuronal tau colocalizing with tubulin marker TUBB3 was dramatically reduced (**Fig. 4L,M**). This suggests that microglia or microglia-derived cues are necessary to promote the observed tau phosphorylation in the context of *APOE4*.

To assess whether secreted factors resultant from microglia-astrocyte crosstalk contribute to the increased tau phosphorylation, we collected conditioned medium from *APOE4* microglia-astrocyte co-culture, treated with the same 20 nM dose of exogenous Aβ-42 for 72 hours, and applied it to *APOE4* miBrains (**Fig. 4N**). In parallel, we collected conditioned medium from monocultured *APOE4* astrocytes as well as from monocultured *APOE4* iMG, each treated with 20 nM Aβ-42 for 72 hours, and pooled these media to administer to miBrains (**Fig. 4N**). Interestingly, the co-cultured microglia-astrocyte conditioned medium increased tau phosphorylation while the combined monoculture conditioned media did not (**Fig. 4O,P**). This provides evidence that secreted factors from microglia-astrocyte signaling are sufficient to increase tau phosphorylation, even in the absence of microglia. The extent of tau phosphorylation observed in conditions of microglia-astrocyte co-culture applied to *APOE4* miBrains without iMG was less than that of *APOE4* miBrains with iMG (**Fig. 4L,M**), which could be due to the dose of soluble cues applied or suggest that other iMG-dependent processes contribute to the observed tau phosphorylation. However, the insufficiency of combined monoculture conditioned media compared to microglia-astrocyte co-culture conditioned media to promote tau phosphorylation, suggests that crosstalk between astrocytes and microglia produces factors distinct from their monocultured counterparts that promote neurotoxic phenotypes. These results could be in line with those of a recent study that reported that conditioned media from *APOE4* iMG with high lipid droplet burden, indicative of a pathological state, and not *APOE4* iMG with low levels of lipid droplets nor *APOE3* iMG, promoted tau phosphorylation in primary neuron culture (*67*). It is possible that *APOE4* astrocytes promote a related pathological state in iMG that precipitates neurotoxic phenotypes.

We have thus revealed *APOE4* pathological phenotypes conferred by non-cell autonomous interactions, harnessing the unique utility of our novel miBrain platform to recapitulate multicellular interactions in the CNS and assess cell type-specific phenotypes. Notably, the ability to decouple the genotype of individual glial cell types from that of neurons opens up new lines of inquiry into non-cell autonomous contributions to neurodegeneration that has not yet been possible with organoid technology. We have established this miBrain platform mimicking the brain niche inclusive of BBB, neuronal, myelin, and immune cell components, with enhanced biomimicry in brain tissue architecture, hallmarks of brain physiology and pathology, and transcriptomic signatures. This is the first *in vitro* model to our knowledge that includes all of these features in a

single tissue mimic. To promote *in vivo*-like signatures of cell components we engineered a novel 3D hydrogel inspired by the composition of the brain interstitial matrix. Neuromatrix, a dextran-based hydrogel incorporating brain-matrix specific protein biochemical cues like versican, enables the vascularized, multicellular co-culture while promoting neuronal activity. The biomaterial design strategy we here undertook could also inform the construction of vascularized tissues for other tissue types. Encapsulating iPSC-derived brain cell types, for each of the six major cell types in the human brain, into Neuromatrix leads to a multicellular co-culture system stable for weeks. Notably, this is the first co-culture to our knowledge stably supporting six different cell types. miBrains recapitulate AD pathological hallmarks of amyloid accumulation and tau phosphorylation and can be used to dissect pathological mechanisms, including cell type-specific mechanisms for any of the component cell types. Furthermore, the assays and evaluation toolbox we have developed are readily deployable to study a broad range of questions and for therapeutic evaluation. While we here incorporated cells from the best iPSC differentiation protocols available, future iterations of the miBrain can integrate any advancements in the iPSC field, including in additional subtypes of neurons. Advancing brain-mimicry *in vitro*, the miBrain platform could be a vehicle for accelerated mechanistic inquiry and therapeutic development for AD as well as other neurological indications.

References and Notes

1. M. A. Lancaster, M. Renner, C.-A. Martin, D. Wenzel, L. S. Bicknell, M. E. Hurles, T. Homfray, J. M. Penninger, A. P. Jackson, J. A. Knoblich, Cerebral organoids model human brain development and microcephaly. *Nature*. **501**, 373–379 (2013).

2. A. M. Paşca, S. A. Sloan, L. E. Clarke, Y. Tian, C. D. Makinson, N. Huber, C. H. Kim, J.-Y. Park, N. A. O'Rourke, K. D. Nguyen, S. J. Smith, J. R. Huguenard, D. H. Geschwind, B. A. Barres, S. P. Paşca, Functional cortical neurons and astrocytes from human pluripotent stem cells in 3D culture. *Nat. Methods*. **12**, 671–678 (2015).

3. G. Quadrato, T. Nguyen, E. Z. Macosko, J. L. Sherwood, S. M. Yang, D. R. Berger, N. Maria, J. Scholvin, M. Goldman, J. P. Kinney, E. S. Boyden, J. W. Lichtman, Z. M. Williams, S. A. McCarroll, P. Arlotta, Cell diversity and network dynamics in photosensitive human brain organoids. *Nature*. **545**, 48–53 (2017).

4. G. Adriani, D. Ma, A. Pavesi, R. D. Kamm, E. L. K. Goh, A 3D neurovascular microfluidic model consisting of neurons, astrocytes and cerebral endothelial cells as a blood-brain barrier. *Lab Chip*. **17**, 448–459 (2017).

5. M. Campisi, Y. Shin, T. Osaki, C. Hajal, V. Chiono, R. D. Kamm, 3D self-organized microvascular model of the human blood-brain barrier with endothelial cells, pericytes and astrocytes. *Biomaterials*. **180**, 117–129 (2018).

6. A. Herland, A. D. Van Der Meer, E. A. FitzGerald, T. E. Park, J. J. F. Sleeboom, D. E. Ingber, Distinct contributions of astrocytes and pericytes to neuroinflammation identified in a 3D human blood-brain barrier on a chip. *PLoS One*. **11**, 1–21 (2016).

7. C. D'Avanzo, J. Aronson, Y. H. Kim, S. H. Choi, R. E. Tanzi, D. Y. Kim, Alzheimer's in 3D culture: Challenges and perspectives. *BioEssays*. **37**, 1139–1148 (2015).

8. T. M. Dawson, T. E. Golde, C. Lagier-Tourenne, Animal models of neurodegenerative diseases. *Nat. Neurosci.* **21**, 1370–1379 (2018).

9. R. M. Ransohoff, All (animal) models (of neurodegeneration) are wrong. Are they also useful? *J. Exp. Med.* **215**, 2955–2958 (2018).

10. K. Takahashi, S. Yamanaka, Induction of Pluripotent Stem Cells from Mouse Embryonic and Adult Fibroblast Cultures by Defined Factors. *Cell*. **126**, 663–676 (2006).

11. P. Karagiannis, K. Takahashi, M. Saito, Y. Yoshida, K. Okita, A. Watanabe, H. Inoue, J. K. Yamashita, M. Todani, M. Nakagawa, M. Osawa, Y. Yashiro, S. Yamanaka, K. Osafune, Induced Pluripotent Stem Cells and Their Use in Human Models of Disease and Development. *Physiol. Rev.* **99**, 79–114 (2019).

12. R. M. Marton, Y. Miura, S. A. Sloan, Q. Li, O. Revah, R. J. Levy, J. R. Huguenard, S. P. Pașca, Differentiation and maturation of oligodendrocytes in human three-dimensional neural cultures. *Nat. Neurosci.* **22**, 484–491 (2019).

13. M. L. Moya, Y.-H. Hsu, A. P. Lee, C. C. W. Hughes, S. C. George, In Vitro Perfused Human Capillary Networks. *Tissue Eng. Part C Methods*. **19**, 730–737 (2013).

14. S. H. Choi, Y. H. Kim, M. Hebisch, C. Sliwinski, S. Lee, C. D'Avanzo, H. Chen, B. Hooli, C. Asselin, J. Muffat, J. B. Klee, C. Zhang, B. J. Wainger, M. Peitz, D. M. Kovacs, C. J. Woolf, S. L. Wagner, R. E. Tanzi, D. Y. Kim, A three-dimensional human neural cell culture model of Alzheimer's disease. *Nature*. **515**, 274–278 (2014).

15. R. M. Linville, J. G. DeStefano, M. B. Sklar, Z. Xu, A. M. Farrell, M. I. Bogorad, C. Chu, P. Walczak, L. Cheng, V. Mahairaki, K. A. Whartenby, P. A. Calabresi, P. C. Searson, Human iPSC-derived blood-brain barrier microvessels: validation of barrier function and endothelial cell behavior. *Biomaterials*. **190**–**191**, 24–37 (2019).

16. S. R. Guttikonda, L. Sikkema, J. Tchieu, N. Saurat, R. M. Walsh, O. Harschnitz, G. Ciceri, M. Sneeboer, L. Mazutis, M. Setty, P. Zumbo, D. Betel, L. D. de Witte, D. Pe'er, L. Studer, Fully defined human pluripotent stem cell-derived microglia and tri-culture system model C3 production in Alzheimer's disease. *Nat. Neurosci.* **24**, 343–354 (2021).

17. J. W. Blanchard, L. A. Akay, J. Davila-Velderrain, D. von Maydell, H. Mathys, S. M. Davidson, A. Effenberger, C.-Y. Chen, K. Maner-Smith, I. Hajjar, E. A. Ortlund, M. Bula, E. Agbas, A. Ng, X. Jiang, M. Kahn, C. Blanco-Duque, N. Lavoie, L. Liu, R. Reyes, Y.-T. Lin, T. Ko, L. R'Bibo, W. T. Ralvenius, D. A. Bennett, H. P. Cam, M. Kellis, L.-H. Tsai, APOE4 impairs myelination via cholesterol dysregulation in oligodendrocytes. *Nature*. **611**, 769–779 (2022).

18. J. W. Blanchard, M. Bula, J. Davila-Velderrain, L. A. Akay, L. Zhu, A. Frank, M. B. Victor, J. M. Bonner, H. Mathys, Y. T. Lin, T. Ko, D. A. Bennett, H. P. Cam, M. Kellis, L. H. Tsai, Reconstruction of the human blood–brain barrier in vitro reveals a pathogenic mechanism of APOE4 in pericytes. *Nat. Med.* **26**, 952–963 (2020).

19. R. N. Kalaria, Cerebral vessels in ageing and Alzheimer's disease. *Pharmacol. Ther.* **72**, 193–214 (1996).

20. J. J. Rodríguez-Arellano, V. Parpura, R. Zorec, A. Verkhratsky, Astrocytes in physiological aging and Alzheimer's disease. *Neuroscience*. **323**, 170–182 (2016).

21. Z. Cai, M. Xiao, Oligodendrocytes and Alzheimer's disease. *Int. J. Neurosci.* **126**, 97–104 (2016).

22. K. A. Clayton, A. A. Van Enoo, T. Ikezu, Alzheimer's Disease: The Role of Microglia in

Brain Homeostasis and Proteopathy. *Front. Neurosci.* **11** (2017), doi:10.3389/fnins.2017.00680.

23. D. V Hansen, J. E. Hanson, M. Sheng, Microglia in Alzheimer ' s disease. *J. Cell Biol.* **217**, 459–72 (2018).

24. J. Iannucci, W. Renehan, P. Grammas, Thrombin, a Mediator of Coagulation, Inflammation, and Neurotoxicity at the Neurovascular Interface: Implications for Alzheimer's Disease. *Front. Neurosci.* **14** (2020), doi:10.3389/fnins.2020.00762.

25. A. M. Saunders, W. J. Strittmatter, D. Schmechel, P. H. St. George-Hyslop, M. A. Pericak-Vance, S. H. Joo, B. L. Rosi, J. F. Gusella, D. R. Crapper-MacLachlan, M. J. Alberts, C. Hulette, B. Crain, D. Goldgaber, A. D. Roses, Association of apolipoprotein E allele 4 with late-onset familial and sporadic Alzheimer's disease. *Neurology*. **43**, 1467–1467 (1993).

26. A. Aazmi, H. Zhou, W. Lv, M. Yu, X. Xu, H. Yang, Y. S. Zhang, L. Ma, Vascularizing the brain in vitro. *iScience*. **25**, 104110 (2022).

27. C. Patsch, L. Myelan-Challet, E. C. Thoma, E. Urich, T. Heckel, J. F. O-Sullivan, S. J. Grainger, F. G. Kapp, L. Sun, K. Christensen, Y. Xia, M. H. C. Florido, W. He, W. Pan, M. Prummer, C. R. Warren, R. Jakob-Roetne, U. Certa, R. Jagasia, P.-O. Freskgard, I. Adatto, D. Kling, P. Huang, L. I. Zon, E. L. Chaikof, R. E. Gerszten, M. Graf, R. Iacone, C. A. Cowan, Generation of vascular endothelial and smooth muscle cells from human pluripotent stem cells. *Nat. Cell Biol.* **17**, 994–1006 (2015).

28. H. Nishihara, B. D. Gastfriend, P. Kasap, S. P. Palecek, E. V. Shusta, B. Engelhardt, Differentiation of human pluripotent stem cells to brain microvascular endothelial cell-like cells suitable to study immune cell interactions. *STAR Protoc.* **2**, 100563 (2021).

29. P. Douvaras, J. Wang, M. Zimmer, S. Hanchuk, M. O'Bara, S. Sadiq, F. Sim, J. Goldman, V. Fossati, Efficient generation of myelinating oligodendrocytes from primary progressive multiple scelrosis patients by induced pluripotent stem cells. *Stem Cell Reports*. **3**, 250–259 (2014).

30. Y. Zhang, C. H. Pak, Y. Han, H. Ahlenius, Z. Zhang, S. Chanda, S. Marro, C. Patzke, C. Acuna, J. Covy, W. Xu, N. Yang, T. Danko, L. Chen, M. Wernig, T. C. Südhof, Rapid single-step induction of functional neurons from human pluripotent stem cells. *Neuron*. **78**, 785–798 (2013).

31. J. TCW, M. Wang, A. A. Pimenova, K. R. Bowles, B. J. Hartley, E. Lacin, S. I. Machlovi, R. Abdelaal, C. M. Karch, H. Phatnani, P. A. Slesinger, B. Zhang, A. M. Goate, K. J. Brennand, An Efficient Platform for Astrocyte Differentiation from Human Induced Pluripotent Stem Cells. *Stem Cell Reports*. **9**, 600–614 (2017).

32. E. M. Abud, R. N. Ramirez, E. S. Martinez, L. M. Healy, C. H. H. Nguyen, S. A. Newman, A. V. Yeromin, V. M. Scarfone, S. E. Marsh, C. Fimbres, C. A. Caraway, G. M. Fote, A. M. Madany, A. Agrawal, R. Kayed, K. H. Gylys, M. D. Cahalan, B. J. Cummings, J. P. Antel, A. Mortazavi, M. J. Carson, W. W. Poon, M. Blurton-Jones, iPSC-Derived Human Microglia-like Cells to Study Neurological Diseases. *Neuron*. **94**, 278-293.e9 (2017).

33. L. W. Lau, R. Cua, M. B. Keough, S. Haylock-Jacobs, V. W. Yong, Pathophysiology of the brain extracellular matrix: a new target for remyelination. *Nat. Rev. Neurosci.* **14**, 722–

729 (2013).

34. D. Bonneh-Barkay, C. A. Wiley, Brain Extracellular Matrix in Neurodegeneration. *Brain Pathol.* **19**, 573–585 (2009).

35. E. A. Aisenbrey, W. L. Murphy, Synthetic alternatives to Matrigel. *Nat. Rev. Mater.* **5**, 539–551 (2020).

36. S. Möller, J. Weisser, S. Bischoff, M. Schnabelrauch, Dextran and hyaluronan methacrylate based hydrogels as matrices for soft tissue reconstruction. *Biomol. Eng.* **24**, 496–504 (2007).

37. S. Netsopa, S. Niamsanit, D. Sakloetsakun, N. Milintawisamai, Characterization and Rheological Behavior of Dextran from Weissella confusa R003. *Int. J. Polym. Sci.* **2018**, 1–10 (2018).

38. K. Bisht, K. A. Okojie, K. Sharma, D. H. Lentferink, Y. Y. Sun, H. R. Chen, J. O. Uweru, S. Amancherla, Z. Calcuttawala, A. B. Campos-Salazar, B. Corliss, L. Jabbour, J. Benderoth, B. Friestad, W. A. Mills, B. E. Isakson, M. È. Tremblay, C. Y. Kuan, U. B. Eyo, Capillary-associated microglia regulate vascular structure and function through PANX1-P2RY12 coupling in mice. *Nat. Commun.* **12** (2021), doi:10.1038/s41467-021-25590-8.

39. A. Badimon, H. J. Strasburger, P. Ayata, X. Chen, A. Nair, A. Ikegami, P. Hwang, A. T. Chan, S. M. Graves, J. O. Uweru, C. Ledderose, M. G. Kutlu, M. A. Wheeler, A. Kahan, M. Ishikawa, Y. C. Wang, Y. H. E. Loh, J. X. Jiang, D. J. Surmeier, S. C. Robson, W. G. Junger, R. Sebra, E. S. Calipari, P. J. Kenny, U. B. Eyo, M. Colonna, F. J. Quintana, H. Wake, V. Gradinaru, A. Schaefer, Negative feedback control of neuronal activity by microglia. *Nature*. **586**, 417–423 (2020).

40. M. B. Victor, N. Leary, X. Luna, H. S. Meharena, A. N. Scannail, P. L. Bozzelli, G. Samaan, M. H. Murdock, D. von Maydell, A. H. Effenberger, O. Cerit, H.-L. Wen, L. Liu, G. Welch, M. Bonner, L.-H. Tsai, Lipid accumulation induced by APOE4 impairs microglial surveillance of neuronal-network activity. *Cell Stem Cell*. **29**, 1197-1212.e8 (2022).

41. N. J. Abbott, L. Rönnbäck, E. Hansson, Astrocyte-endothelial interactions at the blood-brain barrier. *Nat. Rev. Neurosci.* **7**, 41–53 (2006).

42. M. D. Sweeney, S. Ayyadurai, B. V Zlokovic, Pericytes of the neurovascular unit: key functions and signaling pathways. *Nat. Neurosci.* **19**, 771–783 (2016).

43. M. Prinz, J. Priller, Microglia and brain macrophages in the molecular age: from origin to neuropsychiatric disease. *Nat. Rev. Neurosci.* **15**, 300–312 (2014).

44. T. Philips, J. D. Rothstein, Oligodendroglia: metabolic supporters of neurons. *J. Clin. Invest.* **127**, 3271–3280 (2017).

45. R. A. Harris, L. Tindale, R. C. Cumming, Age-dependent metabolic dysregulation in cancer and Alzheimer's disease. *Biogerontology*. **15**, 559–577 (2014).

46. R. A. Stelzmann, H. Norman Schnitzlein, F. Reed Murtagh, An english translation of alzheimer's 1907 paper, Uber eine eigenartige erkankung der hirnrinde? *Clin. Anat.* **8**, 429–431 (1995).

47. J. A. Lee, B. Hall, J. Allsop, R. Alqarni, S. P. Allen, Lipid metabolism in astrocytic structure and function. *Semin. Cell Dev. Biol.* **112**, 123–136 (2021).

48. Y. T. Lin, J. Seo, F. Gao, H. M. Feldman, H. L. Wen, J. Penney, H. P. Cam, E. Gjoneska, W. K. Raja, J. Cheng, R. Rueda, O. Kritskiy, F. Abdurrob, Z. Peng, B. Milo, C. J. Yu, S. Elmsaouri, D. Dey, T. Ko, B. A. Yankner, L. H. Tsai, APOE4 Causes Widespread Molecular and Cellular Alterations Associated with Alzheimer's Disease Phenotypes in Human iPSC-Derived Brain Cell Types. *Neuron*. **98**, 1141-1154.e7 (2018).

49. G. Sienski, P. Narayan, J. M. Bonner, N. Kory, S. Boland, A. A. Arczewska, W. T. Ralvenius, L. Akay, E. Lockshin, L. He, B. Milo, A. Graziosi, V. Baru, C. A. Lewis, M. Kellis, D. M. Sabatini, L.-H. Tsai, S. Lindquist, APOE4 disrupts intracellular lipid homeostasis in human iPSC-derived glia. *Sci. Transl. Med.* **13**, 1–12 (2021).

50. B. Farmer, J. Kluemper, L. Johnson, Apolipoprotein E4 Alters Astrocyte Fatty Acid Metabolism and Lipid Droplet Formation. *Cells*. **8**, 182 (2019).

51. J. TCW, L. Qian, N. H. Pipalia, M. J. Chao, S. A. Liang, Y. Shi, B. R. Jain, S. E. Bertelsen, M. Kapoor, E. Marcora, E. Sikora, E. J. Andrews, A. C. Martini, C. M. Karch, E. Head, D. M. Holtzman, B. Zhang, M. Wang, F. R. Maxfield, W. W. Poon, A. M. Goate, Cholesterol and matrisome pathways dysregulated in astrocytes and microglia. *Cell*. **185**, 2213-2233.e25 (2022).

52. P. Chatterjee, S. Pedrini, E. Stoops, K. Goozee, V. L. Villemagne, P. R. Asih, I. M. W. Verberk, P. Dave, K. Taddei, H. R. Sohrabi, H. Zetterberg, K. Blennow, C. E. Teunissen, H. M. Vanderstichele, R. N. Martins, Plasma glial fibrillary acidic protein is elevated in cognitively normal older adults at risk of Alzheimer's disease. *Transl. Psychiatry*. **11**, 27 (2021).

53. A. Abdelhak, M. Foschi, S. Abu-Rumeileh, J. K. Yue, L. D'Anna, A. Huss, P. Oeckl, A. C. Ludolph, J. Kuhle, A. Petzold, G. T. Manley, A. J. Green, M. Otto, H. Tumani, Blood GFAP as an emerging biomarker in brain and spinal cord disorders. *Nat. Rev. Neurol.* **18**, 158–172 (2022).

54. E. Raponi, F. Agenes, C. Delphin, N. Assard, J. Baudier, C. Legraverend, J.-C. Deloulme, S100B expression defines a state in which GFAP-expressing cells lose their neural stem cell potential and acquire a more mature developmental stage. *Glia*. **55**, 165–177 (2007).

55. J. Steiner, H.-G. Bernstein, H. Bielau, A. Berndt, R. Brisch, C. Mawrin, G. Keilhoff, B. Bogerts, Evidence for a wide extra-astrocytic distribution of S100B in human brain. *BMC Neurosci.* **8**, 2 (2007).

56. A. Villarreal, R. Seoane, A. González Torres, G. Rosciszewski, M. F. Angelo, A. Rossi, P. A. Barker, A. J. Ramos, S100B protein activates a RAGE-dependent autocrine loop in astrocytes: implications for its role in the propagation of reactive gliosis. *J. Neurochem.* **131**, 190–205 (2014).

57. Y. Chen, C. Qin, J. Huang, X. Tang, C. Liu, K. Huang, J. Xu, G. Guo, A. Tong, L. Zhou, The role of astrocytes in oxidative stress of central nervous system: A mixed blessing. *Cell Prolif.* **53** (2020), doi:10.1111/cpr.12781.

58. M. V. Sofroniew, Molecular dissection of reactive astrogliosis and glial scar formation. *Trends Neurosci.* **32**, 638–647 (2009).

59. H. Chun, H. Im, Y. J. Kang, Y. Kim, J. H. Shin, W. Won, J. Lim, Y. Ju, Y. M. Park, S. Kim, S. E. Lee, J. Lee, J. Woo, Y. Hwang, H. Cho, S. Jo, J.-H. Park, D. Kim, D. Y. Kim, J.-S. Seo, B. J. Gwag, Y. S. Kim, K. D. Park, B.-K. Kaang, H. Cho, H. Ryu, C. J. Lee, Severe reactive astrocytes precipitate pathological hallmarks of Alzheimer's disease via H2O2− production. *Nat. Neurosci.* **23**, 1555–1566 (2020).

60. V. N. Pivtoraiko, S. L. Stone, K. A. Roth, J. J. Shacka, Oxidative Stress and Autophagy in the Regulation of Lysosome-Dependent Neuron Death. *Antioxid. Redox Signal.* **11**, 481–496 (2009).

61. H. Wei, S.-J. Kim, Z. Zhang, P.-C. Tsai, K. E. Wisniewski, A. B. Mukherjee, ER and oxidative stresses are common mediators of apoptosis in both neurodegenerative and non-neurodegenerative lysosomal storage disorders and are alleviated by chemical chaperones. *Hum. Mol. Genet.* **17**, 469–477 (2008).

62. C.-C. Liu, N. Zhao, Y. Fu, N. Wang, C. Linares, C.-W. Tsai, G. Bu, ApoE4 Accelerates Early Seeding of Amyloid Pathology. *Neuron*. **96**, 1024-1032.e3 (2017).

63. Y. Shi, K. Yamada, S. A. Liddelow, S. T. Smith, L. Zhao, W. Luo, R. M. Tsai, S. Spina, L. T. Grinberg, J. C. Rojas, G. Gallardo, K. Wang, J. Roh, G. Robinson, M. B. Finn, H. Jiang, P. M. Sullivan, C. Baufeld, M. W. Wood, C. Sutphen, L. McCue, C. Xiong, J. L. Del-Aguila, J. C. Morris, C. Cruchaga, A. M. Fagan, B. L. Miller, A. L. Boxer, W. W. Seeley, O. Butovsky, B. A. Barres, S. M. Paul, D. M. Holtzman, ApoE4 markedly exacerbates tau-mediated neurodegeneration in a mouse model of tauopathy. *Nature*. **549**, 523–527 (2017).

64. C. Wang, M. Xiong, M. Gratuze, X. Bao, Y. Shi, P. S. Andhey, M. Manis, C. Schroeder, Z. Yin, C. Madore, O. Butovsky, M. Artyomov, J. D. Ulrich, D. M. Holtzman, Selective removal of astrocytic APOE4 strongly protects against tau-mediated neurodegeneration and decreases synaptic phagocytosis by microglia. *Neuron*, 1–18 (2021).

65. S. A. Liddelow, K. A. Guttenplan, L. E. Clarke, F. C. Bennett, C. J. Bohlen, L. Schirmer, M. L. Bennett, A. E. Münch, W.-S. Chung, T. C. Peterson, D. K. Wilton, A. Frouin, B. A. Napier, N. Panicker, M. Kumar, M. S. Buckwalter, D. H. Rowitch, V. L. Dawson, T. M. Dawson, B. Stevens, B. A. Barres, Neurotoxic reactive astrocytes are induced by activated microglia. *Nature*. **541**, 481–487 (2017).

66. M. K. Jha, M. Jo, J.-H. Kim, K. Suk, Microglia-Astrocyte Crosstalk: An Intimate Molecular Conversation. *Neurosci.* **25**, 227–240 (2019).

67. M. S. Haney, C. N. Munson, I. H. Guldner, N. Schaum, K. Calcuttawala, A. Shin, N. Koutsodendris, G. Serrano, T. Beach, E. M. Reiman, T. Wyss-coray, APOE4 / 4 is linked to damaging lipid droplets in Alzheimer ' s microglia. *bioRxiv* (2023) (available at https://www.biorxiv.org/content/10.1101/2023.07.21.549930v1).

68. Y. Yu, Y. Chau, One-Step "Click" Method for Generating Vinyl Sulfone Groups on Hydroxyl-Containing Water-Soluble Polymers. *Biomacromolecules*. **13**, 937–942 (2012).

Acknowledgments: The authors would like to acknowledge the MIT Biology BioMicro Center for performing RNA-sequencing and quality analysis, the MIT Koch Institute Flow Cytometry Core at the Swanson Biotechnology Center for assistance with flow cytometry, and Matheus Victor for providing the mCherry iPSC line. The authors would also like to acknowledge generous support from The JPB Foundation, The Picower Institute for Learning and Memory, The BT Charitable Foundation, the Robert A. and Renee E. Belfer Family, Lester A. Gimpelson, Eduardo Eurnekian, David B. Emmes, Kathleen and Miguel Octavio and, Jay L. And Carroll D. Miller.

Funding:

National Institutes of Health grant 3-UG3-NS115064-01S1 (LHT)

National Institutes of Health grant 1F32AG072813-01 (AES)

Kavanaugh Fellowship (AES)

Picower Fellowship (AB)

Schmidt Science Fellows in partnership with the Rhodes Trust (RLP)

Author contributions:

Conceptualization: LHT, JWB, AES, RSL

Methodology: AES, AB, DSP, BJ

Investigation: AES, AB, EA, BJ, DSP, AJ, RLP, NT, CS

Visualization: AES, AB

Funding acquisition: LHT, JWB, MK, RSL, AES

Project administration: LHT, RSL

Supervision: LHT, RSL

Writing – original draft: AES

Writing – review & editing: AES, LHT, RSL, AB

Competing interests: No competing interests to disclose.

Data and materials availability: All data, code, and materials used in the analysis will be made available upon reasonable request.

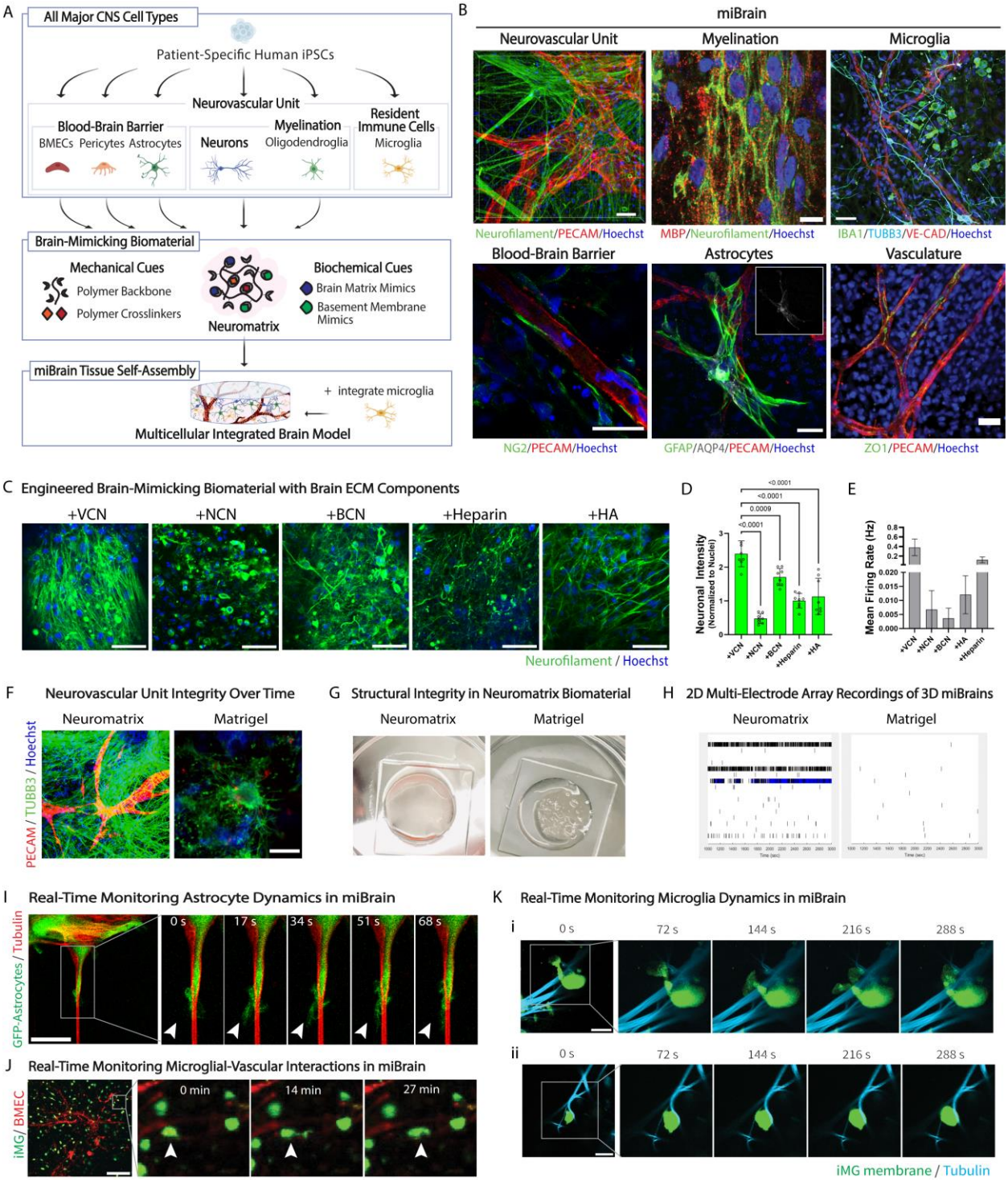

Fig. 1: Human Integrated 3D-Immuno-Glial-Neurovascular miBrain Model. (**A**) Schematic of miBrain formation harnessing patient-specific iPSCs differentiated into each of the resident brain cell types, encapsulated in Neuromatrix hydrogel, and co-cultured for integral cell network self-assembly and microglia-like cell integration, (**B**) miBrains recapitulate key hallmarks of human brain tissue: (*top, left*) neurovascular networks co-assembled into an integral tissue, visualized with an anterior view of a miBrain 3D rendering (red: PECAM, green: neurofilament, blue: Hoechst; scale bar, 50 µm), (*top, middle*) myelination of neuronal projections (red: MBP,

green: neurofilament, blue: Hoechst; scale bar, 10 µm), (*top, right*) integration of iPSC-derived microglia into miBrains (green: IBA1, cyan: TUBB3, red: VE-CAD, blue: Hoechst; scale bar, 50 µm), (*bottom, left*) BBB phenotypes with pericytes localized to the vessels (green: NG2, red: PECAM, blue: Hoechst; scale bar, 30 µm), (*bottom, middle*) astrocytes with end-feet extending to vessels expressing canonical aquaporin-4 transporter (green: GFAP, gray: AQP4, red: PECAM, blue: Hoechst; scale bar, 30 µm; insert, gray: AQP4), (*bottom, right*) ZO-1 tight junctions along vessels (green: ZO-1, red: PECAM, blue: Hoechst; scale bar, 30 µm), (**C**) neuronal phenotypes in miBrains cultured in dextran-based hydrogels fabricated with various brain ECM proteins (green: neurofilament, blue: DAPI; scale bars, 50 µm), (**D**) quantification of neurofilament immunoreactivity (averages of n = 8 samples from n = 3 fields of view per sample), (**E**) neuronal firing as assessed on an MEA system across conditions (n = 3 wells per group, displayed as mean and S.E.M.), (**F**) persistence of neurovascular unit phenotypes in miBrains cultured in Neuromatrix versus Matrigel after 5 weeks in culture (red: PECAM, green: Tuj1, blue: Hoechst; scale bar, 50 µm), (**G**) macroscopic view of gel structural integrity for miBrains cultured in VCN-incorporated engineered dextran-based hydrogel named Neuromatrix hydrogel versus Matrigel after 4 weeks, (**H**) example raster plots from MEA recordings of miBrains in Neuromatrix compared to Matrigel, (**I**) real-time monitoring of astrocyte and neuron dynamics in miBrain over 2 minutes (red: tubulin, green: GFP-Astrocytes; scale bar, 30 µm), (**J**) real-time monitoring of iMG dynamics with vasculature in miBrain over 27 minutes (red: mCherry-BMECs, green: GFP-membrane-labeled iMG; scale bar, 250 µm), (**K**) real-time monitoring of iMG dynamics with neurons in miBrains over 5 minute recordings of (i) example 1 and (ii) example 2 (cyan: tubulin, green: GFP-membrane-labeled iMG; scale bar, 30 µm).

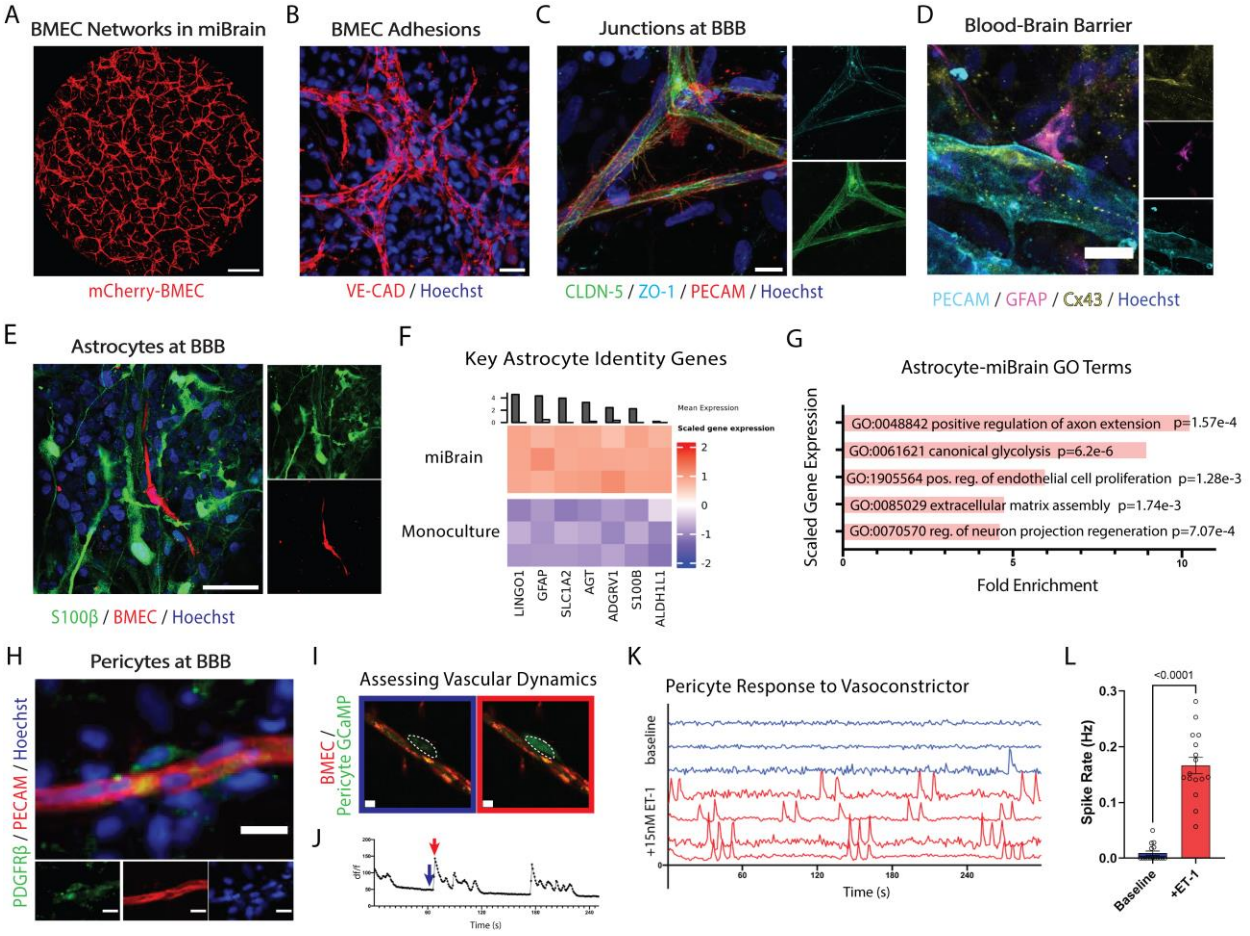

Fig. 2: miBrain promotes brain-mimetic blood-brain barrier phenotypes. (**A**) Integrated emergent networks of endothelial cells in miBrain (red: mCherry-BMECs; scale bar, 500 µm), (**B**) VE-CAD adhesions at vessels (red: VE-CAD, blue: Hoechst; scale bar, 30 µm), (**C**) CLDN-5 tight junctions along vessels (green: CLDN-5, cyan: ZO-1, red: PECAM, blue: Hoechst; scale bar, 100 µm), (**D**) astrocytes at microvasculature and BBB receptor immunohistochemistry at vessels (yellow: Cx43, cyan: PECAM, magenta: GFAP, blue: Hoechst; scale bar, 25 µm), (**E**) immunohistochemistry for astrocytes marker S100β (green: S100β, red: mCherry-BMEC, blue: Hoechst; scale bar, 50 µm), (**F**) expression of key *in vivo*-like genes in astrocytes isolated from miBrain compared to monocultured astrocytes from RNA-sequencing displayed as TMM-normalized and scaled expression for key astrocyte identity genes, (**G**) gene ontology analysis of astrocyte RNAseq for biological pathways upregulated in miBrain-cultured astrocytes based on significantly upregulated and downregulated DEGs and with an FDR p-value less than 0.05, (**H**) pericytes in miBrain localized to the microvascular networks (green: PDGFRβ, red: PECAM, blue: Hoechst; scale bar, 20 µm), (**I**) calcium imaging of pericytes at vessels (left, blue) before and (right, red) during a signaling event (scale bars, 10 µm), (**J**) example traces of calcium transients, (**K**) spike traces (top, blue) with and (bottom, red) without application of vasoconstrictor ET-1, and (**L**) quantification of rate of calcium events (plotting mean and S.E.M., statistical analysis via paired t test).

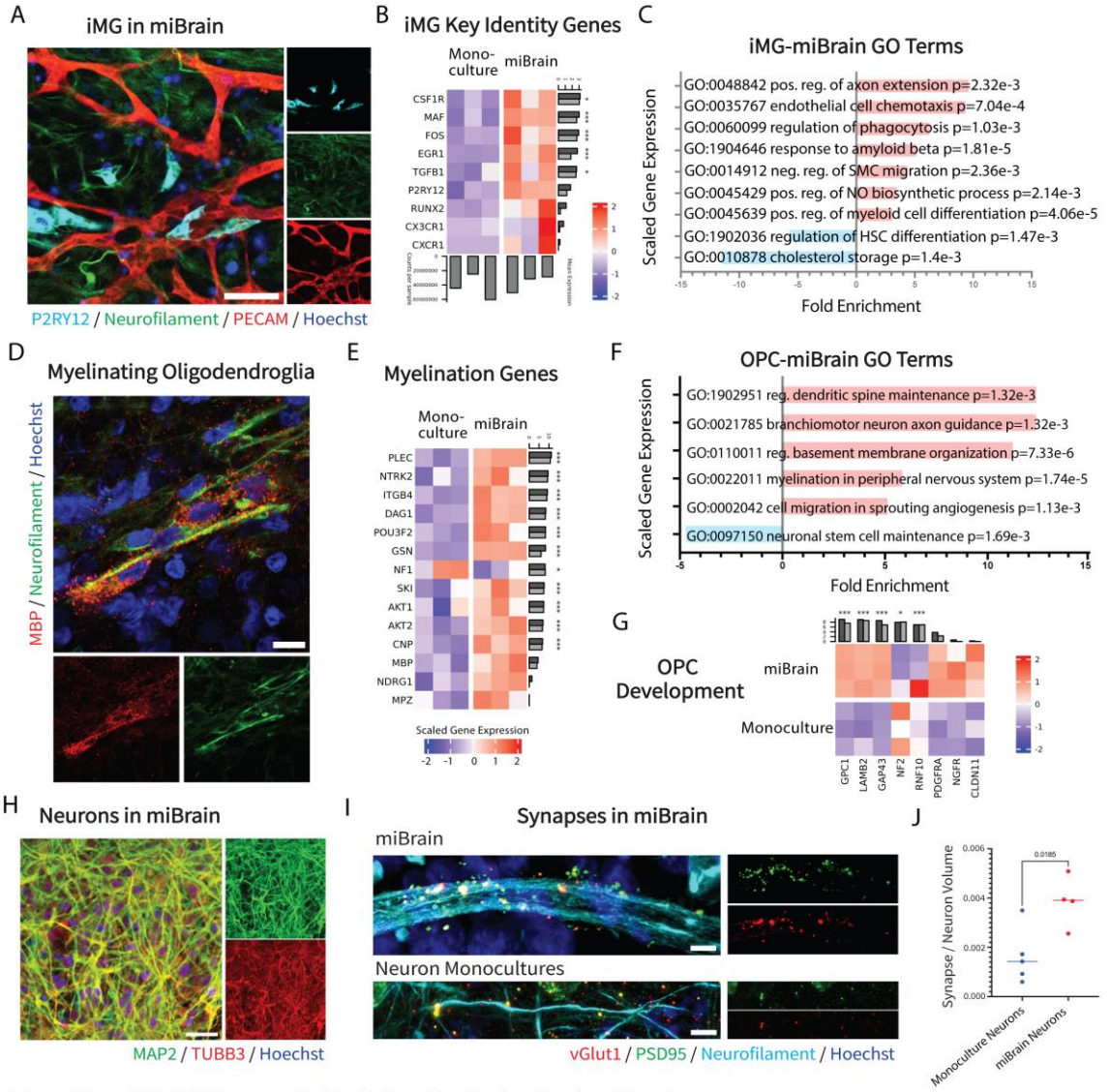

Integration of GCaMP Neurons for Real-Time Monitoring Calcium Transients

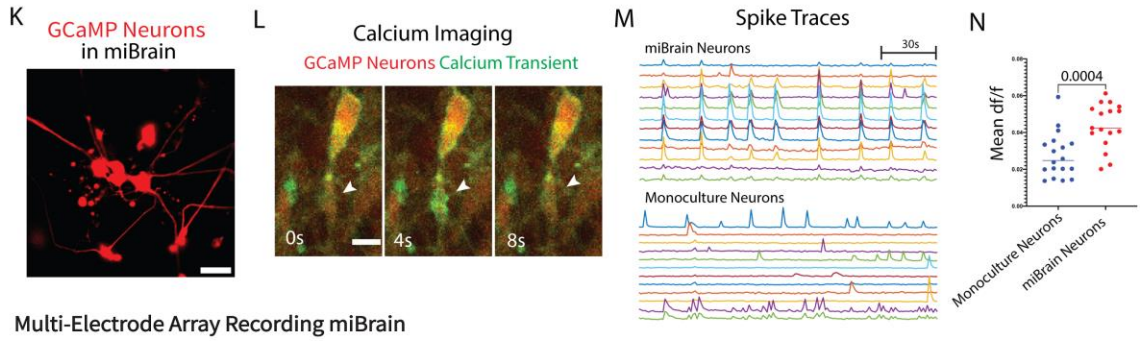

Multi-Electrode Array Recording miBrain

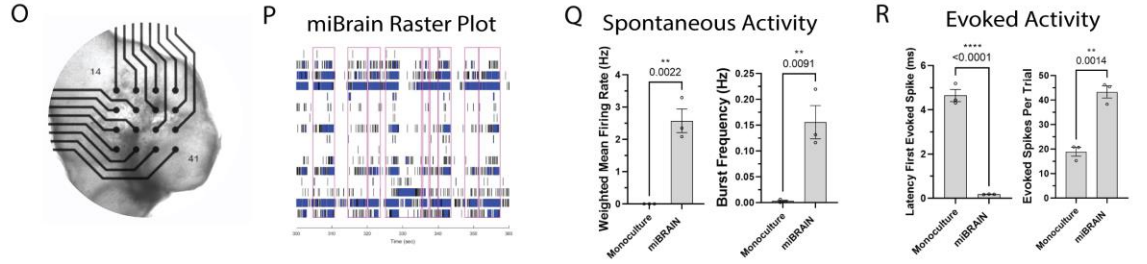

Fig. 3: Neural phenotypes enabled by the miBrain. (**A**) Microglia-like cells in miBrain immunoreactivity to P2RY12 (cyan: P2RY12, green: neurofilament, red: PECAM, blue: Hoechst; scale bar, 50 µm), (**B**) expression of key *in vivo*-like genes in RNAseq of iMG isolated from miBrain compared to monocultured iMG displayed as TMM-normalized and scaled expression (* $p < 0.05$, ** $p < 0.01$, *** $p < 0.001$ for all RNAseq datasets), (**C**) gene ontology analysis of iMG RNAseq for biological pathways significantly altered in miBrain-cultured iMG based on significantly upregulated and downregulated DEGs and with an FDR p-value less than 0.05, (**D**) characterization of myelination produced by oligodendroglia in miBrain via immunohistochemistry (red: MBP, green: neurofilament, blue: Hoechst; scale bar, 10 µm), (**E**) expression of key genes associated with myelination in RNAseq of oligodendroglia isolated from miBrain compared to monocultured oligodendroglia displayed as TMM-normalized and scaled expression, (**F**) gene ontology analysis of oligodendroglia RNAseq for biological pathways significantly altered in miBrain-cultured oligodendroglia based on significantly upregulated and downregulated DEGs and with an FDR p-value less than 0.05, (**G**) expression of key genes associated with OPC development in RNAseq of oligodendroglia isolated from miBrain compared to monocultured oligodendroglia displayed as TMM-normalized and scaled expression, (**H**) characterization of neurons integrated into miBrain immunohistochemistry (green: MAP2, red: TUBB3, blue: Hoechst; scale bar, 30 µm), (**I**) synapses in miBrain (top) versus neuronal monocultures (bottom) (red: vGlut1, green: PSD95, cyan: neurofilament, blue: Hoechst; scale bar, 5 µm), (**J**) quantification of synapses plotted as number of PSD95/synapsin co-localized puncta per volume neurofilament, $n = 4$, student's t-test $p = 0.0185$), (**K**) integration of GCaMP neurons into miBrain for monitoring neuronal calcium transients (red: GCaMP neurons stably expressing tdTomato; scale bar, 30 µm), (**L**) example images of calcium dynamics in GCaMP neurons (red: tdtomato GCaMP neurons, green: calcium transient; scale bar, 25 µm), (**M**) example spike traces of neuronal calcium transients in miBrain (top) compared to monoculture (bottom) (scale bar, 30s), (**N**) quantification of calcium events plotted as max df/f per calcium trace per neuron recorded (statistical analysis via student t test $p = 0.0004$), (**O**) macroscopic image of miBrain on MEA for monitoring electrical activity, (**P**) example raster plot miBrain at week 10, (**Q**) characterization of spontaneous activity in miBrain compared to neuronal monocultures in terms of weighted mean firing rate (left) and burst frequency (right) (plotted as mean and S.E.M.; statistical analysis as unpaired t test), and (**R**) evoked activity in miBrain compared to neuronal monocultures for latency after stimulation (left) and number of evoked spikes per trial (right) (plotted as mean and S.E.M.; statistical analysis as unpaired t test).

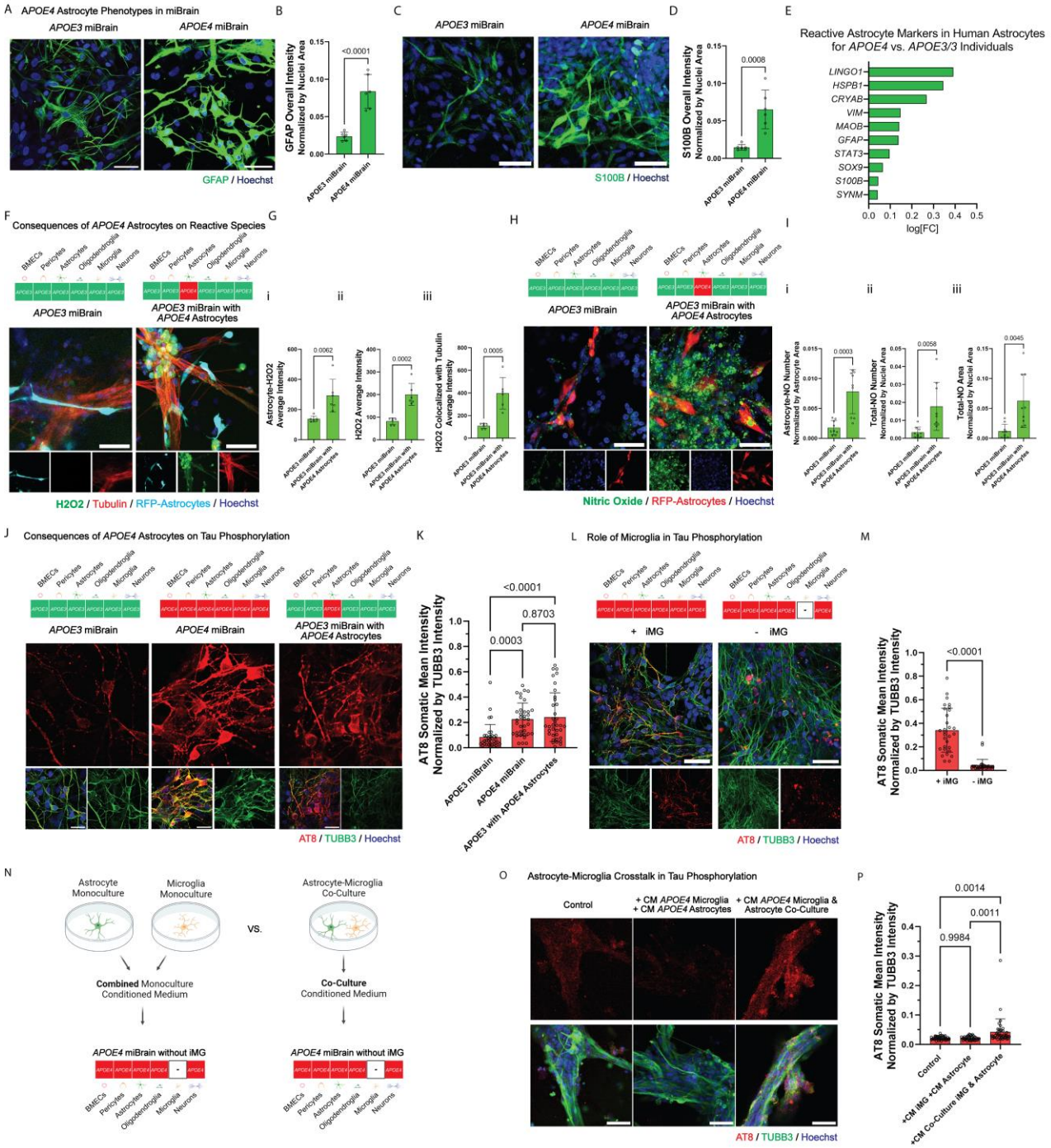

Fig. 4: miBrain Reveals *APOE4* Astrocytes Promote Tau Phosphorylation via Crosstalk with Microglia. (**A**) GFAP immunoreactivity in *APOE3* (left) versus *APOE4* (right) miBrains (green: GFAP, blue: Hoechst; scale bars, 50 µm), (**B**) quantification of GFAP mean intensity normalized by nuclei area (n = 3 samples and images analyzed from n = 6 max projections from confocal z-stacks; statistical analysis by t test), (**C**) S100β immunoreactivity in *APOE3* (left) versus *APOE4* (right) miBrains (green: S100β, blue: Hoechst; scale bars, 50 µm), (**D**) quantification of S100β mean intensity normalized by nuclei area (n = 3 samples and images

analyzed from n = 6 max projections from confocal z-stacks; statistical analysis by t test), (**E**) DEGs in human astrocytes from snRNAseq data set (*cite*) of *APOE3/4* and *APOE4/4* versus *APOE3/3* individuals (positive log[FC] is upregulated in *APOE4*) for genes associated with reactive astrocytes, (**F**) hydrogen peroxide (H2O2) in miBrains with *APOE3* (left) versus *APOE4* (right) astrocytes incorporated into otherwise-*APOE3* miBrains (green: H2O2, red: live tubulin reagent, cyan: RFP-astrocytes, blue: Hoechst; scale bars, 50 µm), (**G**) quantification of hydrogen peroxide in terms of (**i**) mean hydrogen peroxide intensity co-localized with astrocyte region, (**ii**) mean hydrogen peroxide intensity in positive regions, and (**iii**) mean hydrogen peroxide intensity co-localized with tubulin-positive region (data from n = 3 replicates and images from n = 6 max projections from confocal z-stacks; statistical analysis via t test; experiment was conducted in 3 independent trials), (**H**) nitric oxide in miBrains with *APOE3* (left) versus *APOE4* (right) astrocytes incorporated into otherwise-*APOE3* miBrains (green: nitric oxide, red: RFP-astrocytes, blue: Hoechst; scale bars, 50 µm), (**I**) quantification of nitric oxide in terms of (**i**) nitric oxide segmented droplets co-localized with astrocytes normalized by astrocyte area, (**ii**) number of segmented nitric oxide (NO) droplets normalized by the nuclei area, and (**iii**) total area of nitric oxide segmented particles normalized by nuclei area (data from n = 3 replicates and images from n = 9 max projections from confocal z-stacks; statistical analysis via t test; experiment was conducted in 3 independent trials), (**J**) tau phosphorylation in *APOE3* miBrains (left), *APOE4* miBrains (middle), and *APOE3* miBrains with *APOE4* astrocytes (right) for miBrains treated with 20 nM exogenous Aβ 1-42 (red: AT8 phosphorylated tau, green: TUBB3, blue: Hoechst; scale bars, 30 µm), (**K**) quantification of tau phosphorylation assessed in the soma of TUBB3-positive neurons (mean intensity of AT8 normalized by mean intensity of TUBB3 per cell; data from n = 3 replicates and images from n = 12 fields of view; statistical analysis via ANOVA; experiment was conducted in 3 independent trials), (**L**) tau phosphorylation in *APOE4* miBrains with iMG (left) versus without iMG (right) for miBrains treated with 20 nM exogenous Aβ 1-42 (red: AT8 phosphorylated tau, green: TUBB3, blue: Hoechst; scale bars, 50 µm), (**M**) quantification of tau phosphorylation assessed in the soma of TUBB3-positive neurons (mean intensity of AT8 normalized by mean intensity of TUBB3 per cell; data from n = 3 replicates and images from n = 12 fields of view; statistical analysis via t test; experiment was conducted in 3 independent trials), (**N**) schematic illustrating experimental design for testing the effect of *APOE4* microglia-astrocyte crosstalk by collecting conditioned media from astrocyte monocultures and microglia monocultures (top) versus microglia-astrocyte co-culture (center) that is applied to *APOE4* miBrains in the absence of iMG (bottom), (**O**) tau phosphorylation in *APOE4* miBrain controls (left) versus miBrains treated with monoculture CM (middle) versus miBrains treated with microglia-astrocyte co-culture CM (right) co-administered with 20 nM exogenous Aβ 1-42 (red: AT8 phosphorylated tau, green: TUBB3, blue: Hoechst; scale bars, 50 µm), and (**P**) quantification of tau phosphorylation assessed in the soma of TUBB3-positive neurons (mean intensity of AT8 normalized by mean intensity of TUBB3 per cell; data from n = 3 replicates and images from n = 12 fields of view; statistical analysis via ANOVA).

Supplementary Materials

Fig. S1: Differentiation and Validation of iPSC-Derived Brain Cell Types.
Fig. S2: Engineering a Brain-Mimicking Hydrogel for Multicellular miBrain Co-Culture.
Fig. S3: Brain Extracellular Matrix Components Incorporated into Engineered Hydrogel to Enhance Neuronal Phenotypes.
Fig. S4: Transcriptomic Analysis of miBrain-Astrocytes.
Fig. S5: Transcriptomic Analysis of miBrain-iMG.
Fig. S6: Transcriptomic Analysis of miBrain-Oligodendroglia.
Fig. S7: Transcriptomic Analysis of miBrain-Neurons.
Fig. S8: *APOE4* Astrocyte Dysregulation in miBrain.
Fig. S9: Endogenous amyloid and tau pathologies in *APOE4* miBrain.

Materials and Methods

Cell culture

BMECs were differentiated following a protocol similar to previously published protocols (*27*, *28*), with modifications. In brief, on day 0, iPSCs were dissociated to a single-cell suspension and seeded onto basement membrane-grade Matrigel-coated plates at a density of 10,000 cells/cm^2 in mTeSR1 supplemented with 10 µM ROCK inhibitor Y-27632. On day 1, medium was replaced with priming medium (DMEM/F12 media with GlutaMAX, 2% v/v MEM non-essential amino acids, and 1% v/v penicillin:streptomycin) supplemented with 6 µM CHIR-99021 and 10 ng/mL BMP4, feeding daily. On day 4, medium was replaced with endothelial induction medium (hECSR media, 2% v/v B27 supplement, 2% v/v MEM non-essential amino acids, and 1% v/v penicillin:streptomycin) supplemented with 50 ng/mL VEGF-A and 2 µM forskolin, feeding daily. On day 6, cells were passaged onto collagen-coated plates (50 µg/mL collagen type IV diluted in DPBS, coated for a minimum of 30 min at room temperature, then washed once with DPBS prior to use) at a split ratio of 1:3 in endothelial induction medium supplemented with 50 ng/mL VEGF-A and 2 µM forskolin, fed daily. On day 8, cells were passaged by incubating with StemPro Accutase for only ~3-4 min to selectively dissociate endothelial cells, and replated onto collagen-coated plates at a split ratio of 1:5 in endothelial maintenance medium (hECSR media, 2% v/v B27 supplement, 2% v/v MEM non-essential amino acids, 1% v/v penicillin:streptomycin, 10 ng/mL VEGF-A). Cells were fed daily with endothelial maintenance medium and passaged as needed prior to reaching approximately 80% confluency to maintain endothelial cell character. After day 10, expression of endothelial cell-specific marker PECAM was assessed using flow cytometry prior to incorporation into the miBrain (**Fig. S1B**). Absence of pericyte marker PDGFRβ and epithelial cell marker EPCAM, in addition to presence of microvascular marker CD34, were further confirmed by flow cytometry (**Fig. S1B**).

iPSCs were differentiated into pericytes as previously described (*27*). In brief, iPSCs were maintained under feeder-free conditions until colonies reached approximately 80% confluence. On day 0, cells were dissociated using accutase and seeded on hES-grade Matrigel coated plates

at a density of 3,000 cells/ cm^2 and fed with mTeSR media supplemented with 10 μM ROCK inhibitor Y-27632. On day 1, media was replaced with priming media (DMEM/F12 media, 8 μM CHIR-99021, 25 ng/mL BMP4). On day 4, media was replaced with pericyte induction media (DMEM/F12 media, 100 ng/mL PDGF-B, 100 ng/mL activin A). On day 5, cells were passaged using accutase and replated on Matrigel coated plates at a density of $1e^5$ cells/ well of a 6-well plate and fed with pericyte induction media supplemented with 10 μM ROCK inhibitor. Pericytes were maintained without passage for an additional 14 days, feeding with pericyte expansion media (DMEM/F12 media, 10 ng/ml PDGF-B) every two days. Expression of pericyte-specific marker PDGFRβ was assessed using flow cytometry prior to incorporation into miBrains (**Fig. S1D**).

Astrocytes were generated according to a previously published protocol (*31*). Positive expression of astrocyte marker S100β and negative expression of neuronal progenitor marker SOX10 were validated using immunohistochemistry prior to incorporation into miBrain co-cultures (**Fig. S1E**). OPCs were generated according to the protocol described in (*29*). Positive expression of OPC markers PDGFRα and O4 were validated using FACS and immunohistochemistry prior to incorporation into miBrain co-cultures (**Fig. SG,H**). iMG were generated according a previously published protocol (*32*). Positive expression of microglia marker CD45 was validated using FACS prior to incorporation into miBrain co-cultures (**Fig. S1J**). Neurons were differentiated according to a previously published protocol (*30*).

Validated iPSC-differentiated cells were co-cultured in miBrains at the following ratios: 5 M/mL BMECs, 0.25 M/L pericytes, 1 M/mL astrocytes, 1 M/mL OPCs, 5 M/mL neurons, and 2.5 M/mL iMG. miBrains were cultured in Human Endothelial Serum-Free Medium (ThermoFisher Scientific) with 1% pen/strep (Sigma-Aldrich), 1% NEAA (ThermoFisher Scientific), 1% CD lipids (ThermoFisher Scientific), 1% Astrocyte Growth Supplement (ScienCell), 2% B-27 (ThermoFisher Scientific), 10 μL/ mL Insulin (ThermoFisher Scientific), 1 μM db-cAMP (Sigma Aldrich), 50 μg/ mL Ascorbic Acid (Sigma Aldrich), 10 ng/ mL NT-3 (PeproTech), 10 ng/ mL IGF-I (PeproTech), 100 ng/ mL Biotin (Sigma Aldrich), 60 ng/mL T3 (Sigma Aldrich), 4 μg/ mL Folic Acid (Sigma Aldrich) supplemented, 1 μM SAG (Tocris), and 50 ng/ mL VEGF-A (PeproTech). Upon the incorporation of iMG, 25 ng/mL M-CSF (Sigma Aldrich) was added and maintained in the media and after week 2, VEGF-A concentration was reduced to 10 ng/mL.

Neuromatrix hydrogel encapsulation and miBrain formation

BMECs, pericytes, astrocytes, OPCs, and neurons were dissociated with accutase and counted using an automated cell counter (Countess). Cells were encapsulated in Neuromatrix hydrogel precursor solution adapting a dextran hydrogel protocol (*68*), in which 3 mmol/L thiol-reactive groups of 2000 kDa Dextran-VS (Nanocs) or TRUE dextran (Sigma) were reacted with equimolar cell-degradable peptide containing sequence KCGPQGIWGQCK (GenScript), 3.0 mM CRGDS basement membrane-mimicking peptide (GenScript), and 50 μg/ mL human recombinant versican (R&D Systems), after bringing the solution to neutral pH. Cells resuspended in Neuromatrix were dispensed into the bottom of 48-well glass bottom plates (MatTek), allowed to polymerize at 37°C for 25 minutes, and then submerged in miBrain cell

culture medium. The medium was exchanged after one hour to remove any reaction byproducts. miBrains were maintained in culture by feeding every other day. Experiments were performed between weeks 2 and 4 unless otherwise stated.

Immunohistochemistry and confocal imaging

For immunohistochemistry on cell monocultures, cells were passaged onto Matrigel-coated chamber slides (MatTek) and fixed for 20 minutes in 4% PFA, washed with PBS, permeabilized in PBST (PBS, 0.1% Tween-20) for 10 minutes, incubated in blocking solution (PBS, 3% BSA, 2% donkey serum) for 30 minutes, incubated with primary antibody (1:500 unless otherwise specified) for 1 hour at room temperature or overnight at 4°C, washed five times with PBS and incubated with secondary antibody (1:500) and Hoechst 33342 (1:1000) in blocking solution for one hour at room temperature, then washed another five times.

For miBrain immunohistochemistry, miBrains were fixed for 20 minutes in 4% PFA, washed with PBS, permeabilized in PBST (PBS, 0.1% Tween-20) for 30 minutes, incubated in blocking solution (PBS, 3% BSA, 2% donkey serum) for 2 hours, incubated with primary antibody (1:500 unless otherwise specified) overnight at 4°C, washed five times with PBS for a minimum of 15 minutes total and incubated with secondary antibody (1:500) and Hoechst 33342 (1:1000) in blocking solution for one hour at room temperature, and then washed another five times for a minimum of 15 minutes total.

Imaging was performed using a Zeiss LSM 900 confocal microscope.

Antibodies

Primary antibodies for immunohistochemistry used are as follows unless otherwise specified:

Target	Host	Vendor Information	Dilution
Neurofilament (smi311)	mouse	BioLegend 837802	1:500
IBA1	guinea pig	Synaptic Systems 234 004	1:500
Tubulin (TUBB3, TUJ1)	rabbit, mouse	BioLegend 802001, 801213	1:500
NG2	rabbit	Abcam ab255811	1:500
Aquaporin4 (AQP4)	rabbit	Thermo Fisher PA5-53234	1:500
Myelin Basic Protein (MBP)	chicken	Millipore AB9348	1:500
VE-Cadherin (VE-CAD)	goat	R&D Systems AF938	1:500
ZO-1	mouse	Thermo Fisher MA3-39100-A488	1:500
Claudin 5 (CLDN-5)	rabbit	Abcam ab15106	1:500
PECAM	sheep	Biotechne AF806	1:500
GFAP	goat	Abcam ab53554	1:500
Connexin 43 (Cx43)	rabbit	Abcam ab11370	1:500
S100β	rabbit	Abcam ab41548	1:500
P2RY12	rat	BioLegend 848002	1:500
MAP2	chicken	BioLegend 822501	1:500
vGlut1	chicken	Synaptic Systems 135316	1:500
PSD95	rabbit	Abcam ab18258	1:500
Phospho-Tau (AT8)	mouse	Thermo Fisher MN1020	1:500
PDGFRβ	mouse	Abcam ab69506	1:500
SOX2	goat	R&D Systems AF2018	1:500
O4	mouse	Millipore MAB345	1:500

Synapsin	guinea pig	Synaptic Systems 106104	1:500
Oct4	rabbit	Cell Signaling Technology 2890	1:500
Amyloid 82E1	mouse	Immuno-Biological Laboratories 10323	1:500

Corresponding Alexa secondary antibodies (ThermoFisher) were used at 1:500.

Flow cytometry

Cells were dissociated using accutase and washed with FACS buffer (DPBS, 0.5% BSA, 2 mM EDTA), filtered through a 40 µm cell strainer, then resuspended in blocking buffer (DPBS, 1% FBS) with 1:200 antibody and incubated for 25 minutes on ice protected from light. Cells were then washed with FACS buffer and resuspended in buffer with DAPI before filtering through a 40 µm cell strainer and proceeding with FACS. Flow cytometry was performed on a BD LSRFortessa cell analyzer equipped with 355 nm, 405 nm, 488 nm, 561 nm, and 640 nm lasers. Positive expression of cell type specific markers was assessed relative to isotype controls.

Antibodies used for flow cytometry were as follows:

Target	**Host / Isotype**	**Vendor Information**	**Dilution**
CD31-FITC	Mouse IgG1	BioLegend 303104	1:200
CD140b-PE	Mouse IgG2a	BD 558821	1:200
CD44-APC	Mouse IgG1	BioLegend 338806	1:200
PDGFRα-APC	Moue IgG1	R&D systems FAB1264A	1:200
PSA NCAM-APC	Mouse IgM	Miltenyi Biotec 130-120-437	1:200
CD45-APC/Cy7	Mouse IgG1	BD 561863	1:200
FITC mouse IgG1, k isotype control	Mouse IgG1	BioLegend 400107	1:200
PE mouse IgG2a, k isotype control	Mouse IgG2a	BD 555574	1:200
APC mouse IgG1, k isotyle control	Mouse IgG1	BioLegend 400119	1:200
APC mouse IgM isotype control	Mouse IgM	Miltenyi Biotec 130-122-931	1:200
APC/Cy7 mouse IgG1, k isotype control	Mouse IgG1	BD 557873	1:200
P2RY12-PE	Mouse IgG2a	BioLegend 392103	1:200
PE mouse IgG2a, k isotype control	Mouse IgG2a	BioLegend 400213	1:200

Isolation and RNAseq of cell types from miBrain

To isolate cells from miBrains for RNAseq, miBrains were matured for 2 weeks prior to cell isolation and RNA sequencing. Astrocytes and oligodendrocytes were sorted by incorporating mCherry cell lines for the cell type of interest, iMG were sorted based on CD45-Cy7, and neurons were sorted based on labeling the cell type of interest with pAAV-CAG-tdTomato for 24 hours prior to incorporation into miBrain or monoculture (1:50 dilution, Addgene 59462-AAV1).

To ensure sufficient capture of target cell populations, 15 individual miBrains were pooled per replicate, and three replicates were isolated per experiment. In parallel, corresponding cell monocultures were maintained and sorted using the same parameters. To dissociate miBrains,

samples were washed with PBS, then were incubated for 5-10 minutes in a mixture of accutase, collagenase IV (1:20), and dextranase (1:20). These were triturated 15-20 times with a P1000 pipette to form a homogeneous suspension, then pelleted and washed with DPBS twice. Oligodendroglia were fixed with 4% PFA on ice for 20 minutes to ensure stability. Antibodies were incubated alongside isotype controls at 1:200 to samples on ice for 25 minutes for unfixed cells. Dissociated miBrains and monocultures were resuspended in FACS buffer (DPBS, BSA, EDTA) with DAPI and filtered through a 40 µm strainer. Samples were sorted on a BD FACSAria equipped with a 70 µm nozzle. Cells were gated on FSC-A vs SSC-A to separate intact cells from debris, then FSC-H vs FSC-W and SSC-H vs SSC-W to separate single cells from doublets, then DAPI to exclude dead cells, and then the channel corresponding to the antibody used. Cells were sorted into 96-well plates containing 50 µl RNAprotect per well. Approximately 50,000 cells were collected per replicate. For unfixed cells, RNA was isolated from sorted cells using the Qiagen RNeasy isolation kit according to manufacturer protocols. Standard quality control was performed using AATI fragment analyzer. RNA sequencing libraries were prepared using NEB Ultra II PolyA stranded library and sequenced using Illumina NextSeq500. For fixed samples, sorted cells were spun down and resuspended in 200 µL digestion buffer (RecoverAll kit) supplemented with 1:50 Proteinase K, incubated at 50°C for 15 minutes, and then at 80°C for 15 minutes with no agitation to de-crosslink RNA from fixed tissue. 800 µL Trizol was added to the sample and incubated for 5 minutes, then 215 µl chloroform was added and the sample was vortexed vigorously for 30 seconds. Sample was transferred to a 5-prime phase lock heavy gel tube and centrifuged for 15 minutes at 12,000 g. Upper layer containing RNA was transferred to a fresh 1.5 ml microcentrifuge tube and an equal volume of 100% ethanol before proceeding with RNA isolation using Zymo Direct-zol RNA microprep kit according to manufacturer's instructions. RNA sequencing libraries were prepared using Clontech ZapR kit and sequencing was performed using Illumina NextSeq500.

RNA-sequencing data analysis

RNA-sequencing analysis was performed for each batch in a similar fashion. For preliminary QC, FastQC was used to look at quality. For each sample, gene reads were mapped to GRCh38.p13 and genes to GENCODE v43 using STAR 2.7.9a. These were then counted as reads per-sample using featureCounts from Subread version 1.6.2. Each sample was loaded into R (version 4.2.2) using a BioConductor (version 3.16) based workflow to perform QC and further analysis. Reads were normalized to trimmed mean of M-values (TMM) normalization using the R command "cpm(calcNormFactors(rawCounts, "TMM"))" in edgeR. Differential expression analysis was also performed using edgeR, keeping genes with a threshold of 100 counts per million (CPM) in at least 25% of the samples used in differential expression analysis. The DEGs were calculated in edgeR using a quasi-likelihood F-test with no covariates. Comparisons using a likelihood ratio test (LRT) in edgeR and DESeq2 were performed; but similar results were obtained. Gene ontology analysis was performed on significantly upregulated and downregulated DEGs using Panther DB, which identified GO terms with an FDR p-value less than 0.05. From these GO terms were selected the most biologically salient pathways, presented in order of fold-enrichment.

Calcium imaging of neurons

To generate neurons with GCaMP expression, iPSCs containing tetON Ngn2 were transfected with a plasmid driving GCaMP3 expression under the CAG promoter (Addgene #62810), then differentiated into neurons and incorporated into miBrain cultures as described above. In order to facilitate live imaging, miBrains were cultured on 3-cm glass bottom dishes (MatTek). Two-photon microscopy was performed on an Olympus FVMPE-RS microscope equipped with SpectraPhysics InsightX3 DeepSee laser tuned to 920nm. Images were acquired using Fluoview acquisition software (Olympus), we simultaneously acquired images in the red channel (bandpass filter 575-645 nm) to visualize tdTomato-expressing neurons, and the green channel (bandpass filter 495-540 nm) for GCaMP signal. Time courses of spontaneous calcium activity were collected at various time points, starting at week 4. Regions of interest were defined as tdTomato-positive neuronal soma and were manually outlined using ImageJ software and then quantified in Matlab. Calcium spikes were defined as periods in which GCaMP signal exceeded two standard deviations above baseline.

Calcium imaging of pericytes

To generate pericytes with GCaMP expression, iPSCs were transfected with a lentivirus driving GCaMP6 expression under the CAG promoter, then differentiated into pericytes and incorporated into miBrain cultures together with BMECs generated from an iPSC line with constitutive mCherry expression. Calcium imaging experiments were performed on 2-week old miBrains using the Olympus FVMPE-RS 2-photon microscope as described in the previous section. For vascular dynamics assay, spontaneous activity of pericytes was recorded for approximately 5 minutes, then 100 nM ET-1 was manually injected, followed by a recovery time of 5 minutes before imaging calcium activity for 5 minutes. Regions of interest were defined as pericyte cell bodies and manually outlined using ImageJ software. A calcium transient was defined as a period of time in which mean pericyte calcium signal intensity was greater than two standard deviations above the mean of baseline.

MEA recording

A MaestroPro MEA system (Axion Biosystems) was utilized to record electrical activity on miBrains. miBrains were seeded directly onto MEA plates (Axion Biosystems) and maintained in culture according to our standard protocol. 30 minute recordings were collected from miBrains and analyzed using Neural Metrix software (Axion Biosystems).

Amyloid treatment

Stock solutions of amyloid beta 1-42 peptide (Anaspec) were resuspended in PBS. Peptides were administered to miBrains at 20 nM for three days to induce pathology.

Real-time monitoring miBrain

Live imaging of miBrains were performed on a Zeiss LSM 900 confocal microscope using a 20x objective with environmental control of humidity, temperature, and CO2. Reactive species were

assessed by treating miBrains with biosensors for nitric oxide (siRNO Nitric Oxide Live Cell Dye, Sigma-Aldrich), peroxynitrite (BioTrack 515 Green ONOO-, Sigma-Aldrich), or hydrogen peroxide (Green H2O2, Sigma-Aldrich) following the manufacturer instructions. Mitochondria were similarly assessed using BioTrack 633 Red Mito Dye (Sigma-Aldrich) and lysosomes using BioTrack NIR633 LysO Dye (Sigma-Aldrich). Tubulin was similarly visualized live with a small molecule dye (Cytoskeleton). Astrocytes were labeled for live assays prior to incorporation into miBrains using an AAV (pAAV-CAG-tdTomato, Addgene or AAV9-CAG-GFP, Applied Biological Materials). Microglia were labeled for live assays prior to incorporation using a cell membrane dye (Vybrant Cell-Labeling Solutions, Life Technologies). A stably expressing mCherry cell line was utilized for live imaging endothelial cells that was previously developed using pAAVS1-P-CAG-mCh (Addgene).

Western blots

Whole tissue lysate protein fractions from miBrains were prepared by washing samples with cold PBS, then adding RIPA buffer with protease inhibitor (150µL/sample) (Sigma-Aldrich cat: R0278) and incubating on ice for 20 minutes. Tissue was manually disrupted with a p1000 pipette, then centrifuged at 14,000g for 15 minutes at 4°C. Supernatant containing the protein fraction was then saved and quantified using a Pierce 660 assay (Thermo Fisher cat: 22662). For western analysis, 10 µg of total protein in 6X Laemmli SDS sample buffer (Thermo Fisher Scientific) was heated for 5 minutes at 95°C and subjected to SDS-PAGE. Electrophoresis and transfer onto PVDF membranes was performed using the Biorad Mini-Protean Gel Electrophoresis System and Trans-blot Turbo Transfer System, according to manufacturer recommendations. After transfer, membranes were blocked in TBST (Tris-buffered saline, 0.02% Tween-20) with 5% BSA for 1 hour, and incubated overnight with primary antibody at 4°C in a 1:1000 dilution . After subsequent washes with TBST , membrane was incubated in HRP-linked secondary antibody in a 1:500 dilution for 1 hour . Blots were washed again with TBST, developed with SuperSignal West Pico Chemiluminescent Substrate (Thermo Fisher Scientific), and imaged using the Biorad ChemiDoc MP Imaging System. Protein band densitometry was measured using the FIJI Plot Lanes function as area under the curve, and normalized to the respective internal control (β-Actin) band. Graphs and statistical analysis were performed in GraphPad prism.

Antibodies used for Western blot were as follows:

Target	**Host**	**Catalogue Number**
Phospho-Tau (Ser396)	Rabbit	Invitrogen 44-752G
Tau (4R isoform RD4)	Mouse	Sigma Aldrich 05-804
Tau (HT7)	Mouse	Invitrogen MN1000
β-Actin	Mouse	Sigma Aldrich A5316
β-Actin	Rabbit	Sigma Aldrich ZRB1312
HRP-linked anti-mouse IgG	Sheep	Cytiva NXA931
HRP-linked anti-rabbit IgG	Donkey	Cytiva NA934

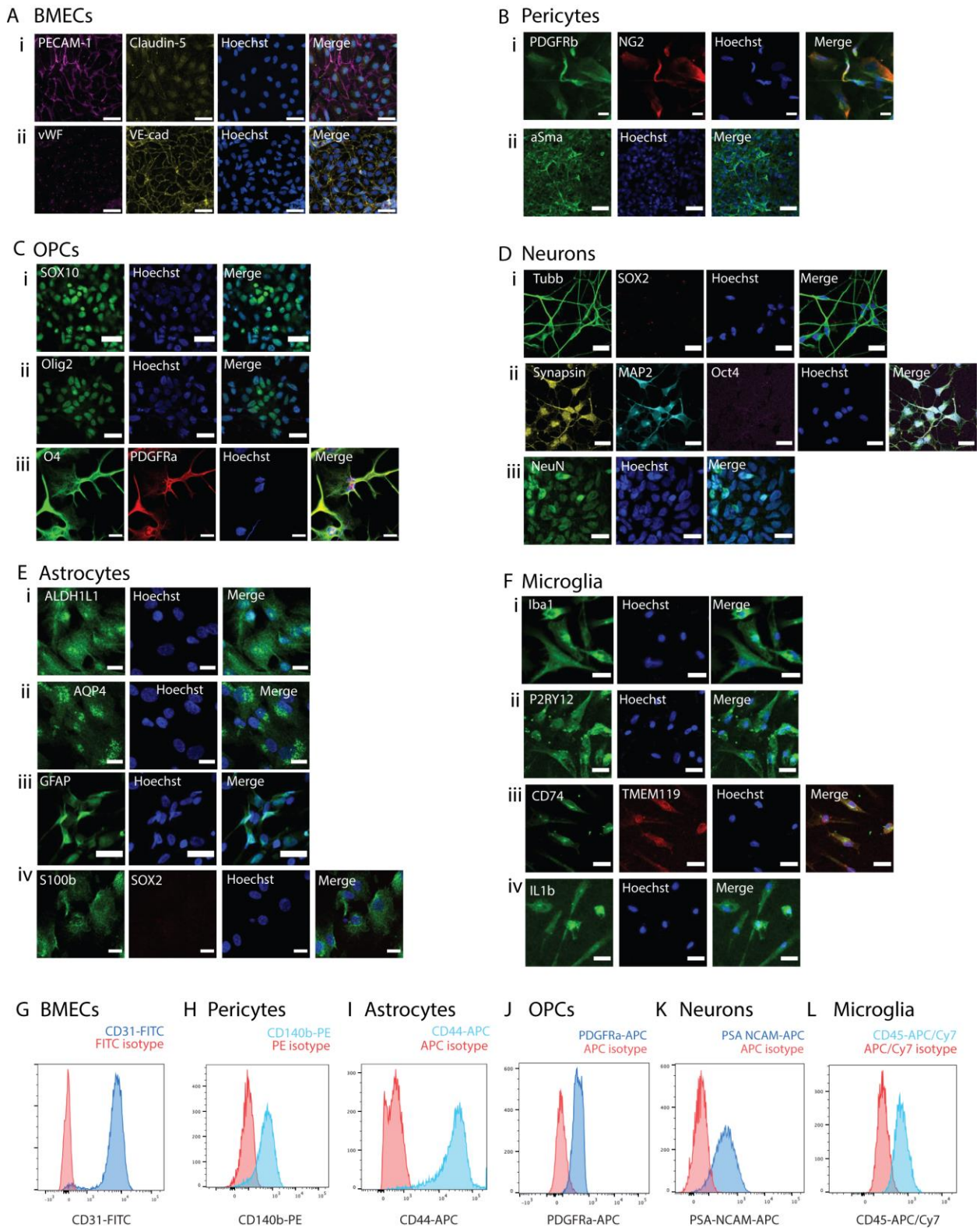

Fig. S1: Differentiation and Validation of iPSC-Derived Brain Cell Types. (**A**) iPSC-derived BMECs immunoreactivity to endothelial cell markers (i) PECAM and Claudin5 (magenta: PECAM, yellow: Claudin5, blue: Hoechst; scale bar, 40 µm), (ii) VWF and VE-CAD (magenta:

VWF, yellow: VE-CAD, blue: Hoechst; scale bar, 40 μm) (**B**) representative immunofluorescence images of iPSC-derived pericytes expressing markers (i) PDGFRβ and NG2 (green: PDGFRβ, red: NG2, blue: Hoechst; scale bars, 20 μm) and (ii) αSMA (green: αSMA, blue: Hoechst; scale bars, 20 μm), (**C**) iPSC-derived OPCs stained positive for markers (i) SOX10 (green: SOX10, blue: Hoechst; scale bar, 20 μm), (ii) Olig2 (green: Olig2, blue: Hoechst; scale bar, 20 μm), and (iii) O4 and PDGFRα (green: O4, red: PDGFRα, blue: Hoechst; scale bar, 20 μm), (**D**) iPSC-derived neurons immunoreactivity (i) to β-Tubulin and SOX2 (red: TUBB, green: SOX2, blue: Hoechst; scale bar, 20 μm), (ii) MAP2 and synapsin and absence of immunoreactivity to pluripotency marker OCT4 (yellow: synapsin, cyan: MAP2, magenta: OCT4, blue: Hoechst; scale bars, 20 μm), and (iii) NeuN (green: NeuN, blue: Hoechst; scale bar, 20 μm), (**E**) iPSC-derived astrocytes positive immunoreactivity to astrocyte markers (i) ALDH1L1 (green: ALDH1L1, blue: Hoechst; scale bar, 20 μm), (ii) AQP4 (green: AQP4, blue: Hoechst; scale bar, 20 μm), (iii) S100β and absence of immunoreactivity to neuron progenitor marker SOX2 (green: S100β, red: SOX2, blue: Hoechst; scale bar, 20 μm), and (iv) GFAP (green: GFAP, red: Nestin, blue: Hoechst; scale bar, 20 μm), and (**F**) iPSC-derived iMG immunoreactivity to canonical markers (i) Iba1 (green: Iba1, blue: Hoechst; scale bar, 20 μm), (ii) P2RY12 (green: P2RY12, blue: Hoechst; scale bar, 20 μm), (iii) TMEM119 (green: CD74, red: TMEM119, blue: Hoechst; scale bar, 20 μm), and (iv) IL1β (green: IL1β, blue: Hoechst; scale bar, 20 μm). (**G**) Flow cytometry of BMECs for canonical marker CD31 (blue: CD31, red: isotype control), (**H**) iPSC-derived pericytes for CD140b (blue: CD140b, red: isotype control), (**I**) iPSC-derived OPCs for PDGFRα (blue: PDGFRα, red: isotype control), (**J**) iPSC-derived neurons for excitatory cortical neuron marker PSA-NCAM (blue: PSA-NCAM, red: isotype control), (**K**) iPSC-derived astrocytes for CD44 (blue: CD44, red: isotype control), and (**L**) iPSC-derived iMG for CD45 (blue: CD45, red: isotype control).

A Matrigel with Brain-Matrix Proteins Incorporated

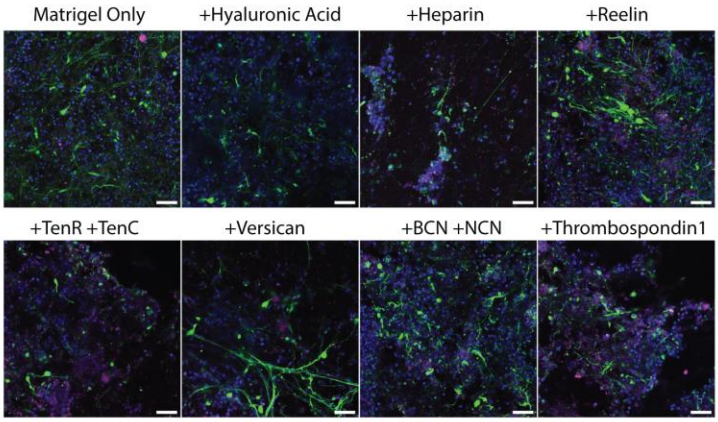

C Matrigel Low Neuronal Activity Even with Brain-Matrix Proteins

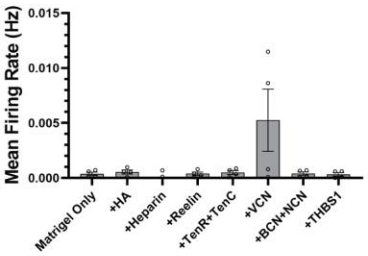

B

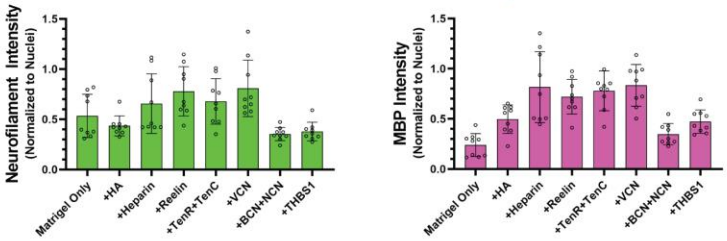

D

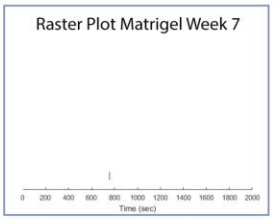

E

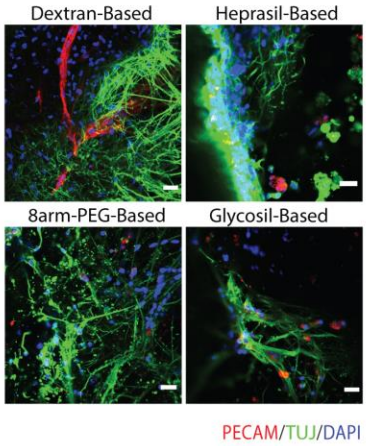

F

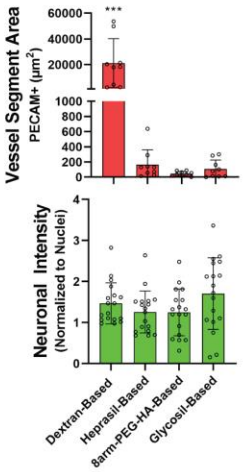

G Electrical Activity in PEG-Based Hydrogels

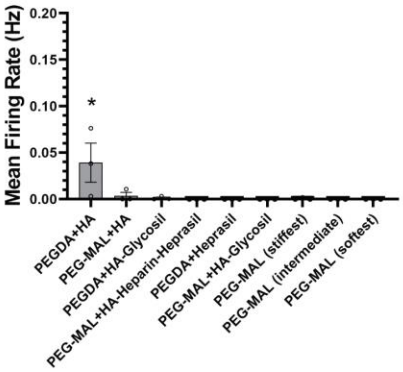

H Optimizing Mechanical Composition for 3D-Neurovascular Unit

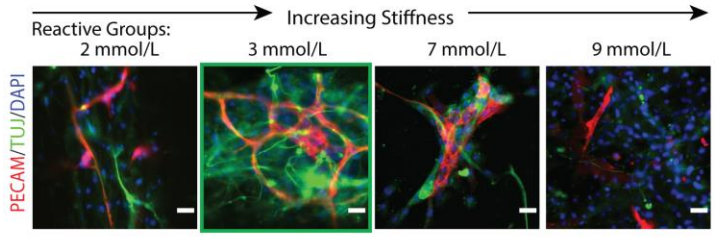

I

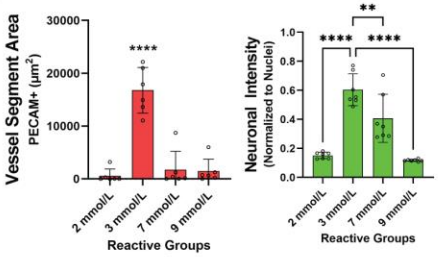

J

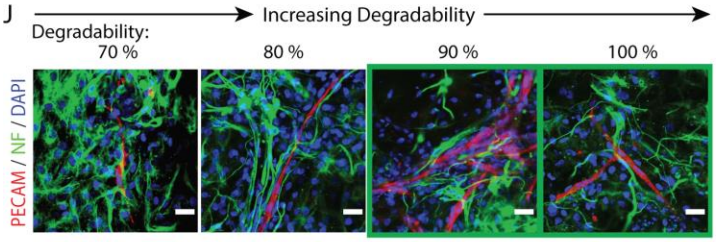

K

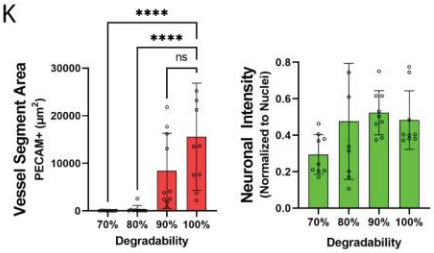

Fig. S2: Engineering a Brain-Mimicking Hydrogel for Multicellular miBrain Co-Culture. (**A**) Neuronal morphology (green: neurofilament) and myelination (magenta: MBP) in miBrains encapsulated in Matrigel incorporated with various brain extracellular matrix proteins (scale bars, 50 µm), (**B**) average intensity of neuronal (top) and MBP immunoreactivity (bottom) across miBrains encapsulated in Matrigel (data from n = 3 replicates, n = 3 fields of view each; plotted as mean and S.D.), (**C**) neuronal activity as measured on an MEA at week 7 for mean firing rate (data from n = 4 replicates, averaged over recordings of at least 30 min.; plotted as mean and S.E.M.), (**D**) raster plot for spikes of neuronal activity in a representative miBrain in Matrigel at week 7, (**E**) neuronal (green: Tuj1) and vessel morphology (red: PECAM) after 2 weeks in culture in various engineered hydrogels (scale bars, 30 µm), (**F**) quantified for area of the segments of vessels (PECAM-positive) captured in images (top; data from n = 3 replicates, n = 3 fields of view each; plotted as mean and S.D.; statistical analysis via one-way ANOVA, *** p = 0.003) and the Tuj1 immunoreactivity (bottom; data from n = 3 replicates, n = 6 fields of view each), (**G**) neuronal activity of miBrains encapsulated in various engineered hydrogels, as assessed by an MEA system after 2 weeks in culture (data from n = 3 replicates, averaged over recordings of at least 30 min.; plotted as mean and S.E.M.; statistical analysis via one-way ANOVA, * p<0.05), (**H**) optimization of mechanical properties of dextran-based hydrogels across amounts of macromer and crosslinker reactive groups, screening across 3D, integral neurovascular network co-assembly for vessels (red: PECAM) and neurons (green: Tuj1) (scale bars, 30 µm), (**I**) quantified in terms of area of the segments of vessels (PECAM+) captured in images (left; data from n = 3 replicates, n = 6 field of view, mean and S.D.; statistical analysis via one-way ANOVA, **** p < 0.0001) and the Tuj1 immunoreactivity (right; data from n = 3 replicates, n = 7 fields of view; statistical analysis via one-way ANOVA, mean and S.D., ** p = 0.006, **** p < 0.0001), (**J**) varying degradability in dextran-based hydrogels, screening across 3D, integral neurovascular network co-assembly for vessels (red: PECAM) and neurons (green: Tuj1) (scale bars, 30 µm), (**K**) quantified in terms of area of the segments of vessels (PECAM+) captured in images (left; data from n = 3 replicates, n = 10 fields of view, mean and S.D.; statistical analysis via one-way ANOVA, **** p < 0.0001) and the Tuj1 immunoreactivity (right; data from n = 3 replicates, n = 3 fields of view each, mean and S.D.).

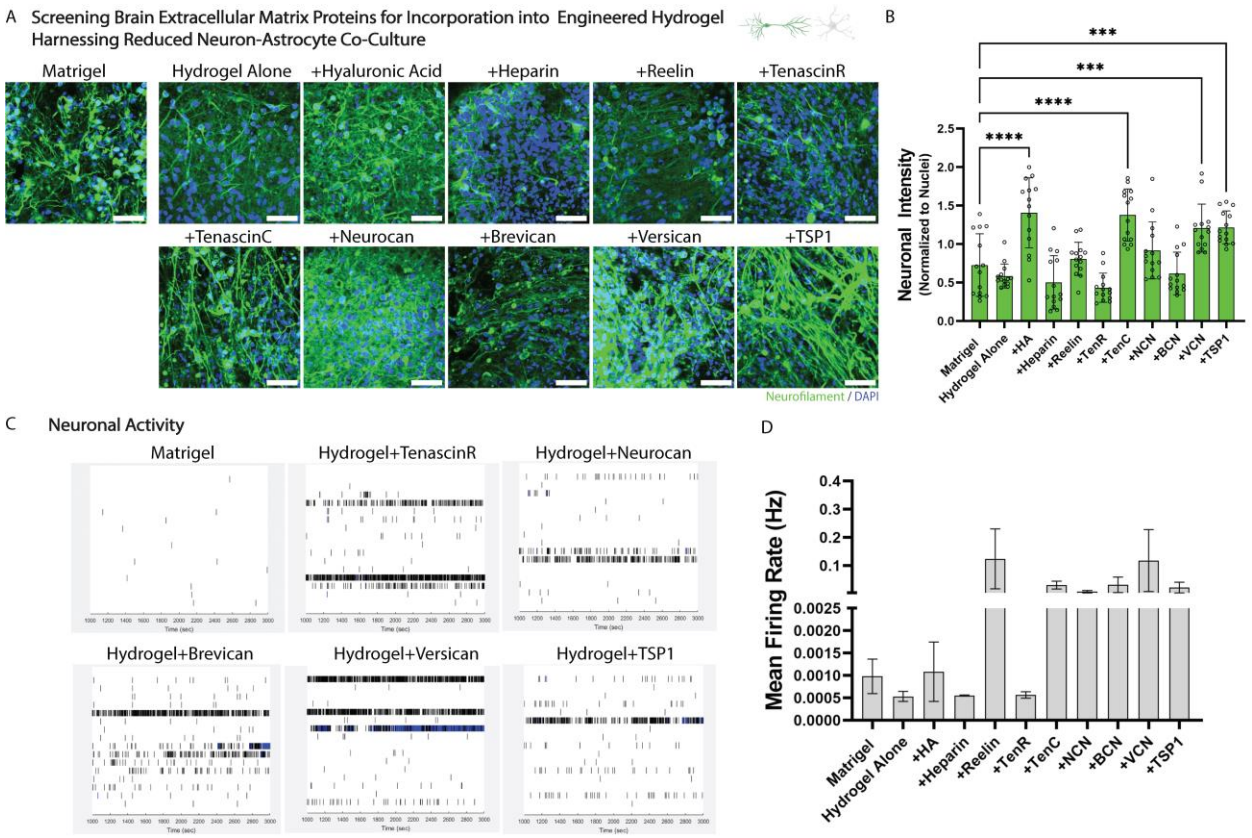

Fig. S3: Brain Extracellular Matrix Components Incorporated into Engineered Hydrogel to Enhance Neuronal Phenotypes. (**A**) Neuronal morphology (green: neurofilament) after 2 weeks in a neuron-astrocyte co-culture used to screen across hydrogels incorporated with various brain extracellular matrix proteins (scale bars, 50 µm), (**B**) average intensity of neuronal immunoreactivity across conditions (data from n = 3 replicates, n = 14 fields of view; statistical analysis via one-way ANOVA, *** $p = 0.006$, **** $p < 0.0001$), (**C**) example raster plots of neuronal activity assessed on an MEA system early in the culture at week 2, and (**D**) averaged mean firing rate at week 2 across extracellular matrix conditions (data are from n = 3 replicates, averaged over recordings of at least 30 min.; mean and S.E.M.).

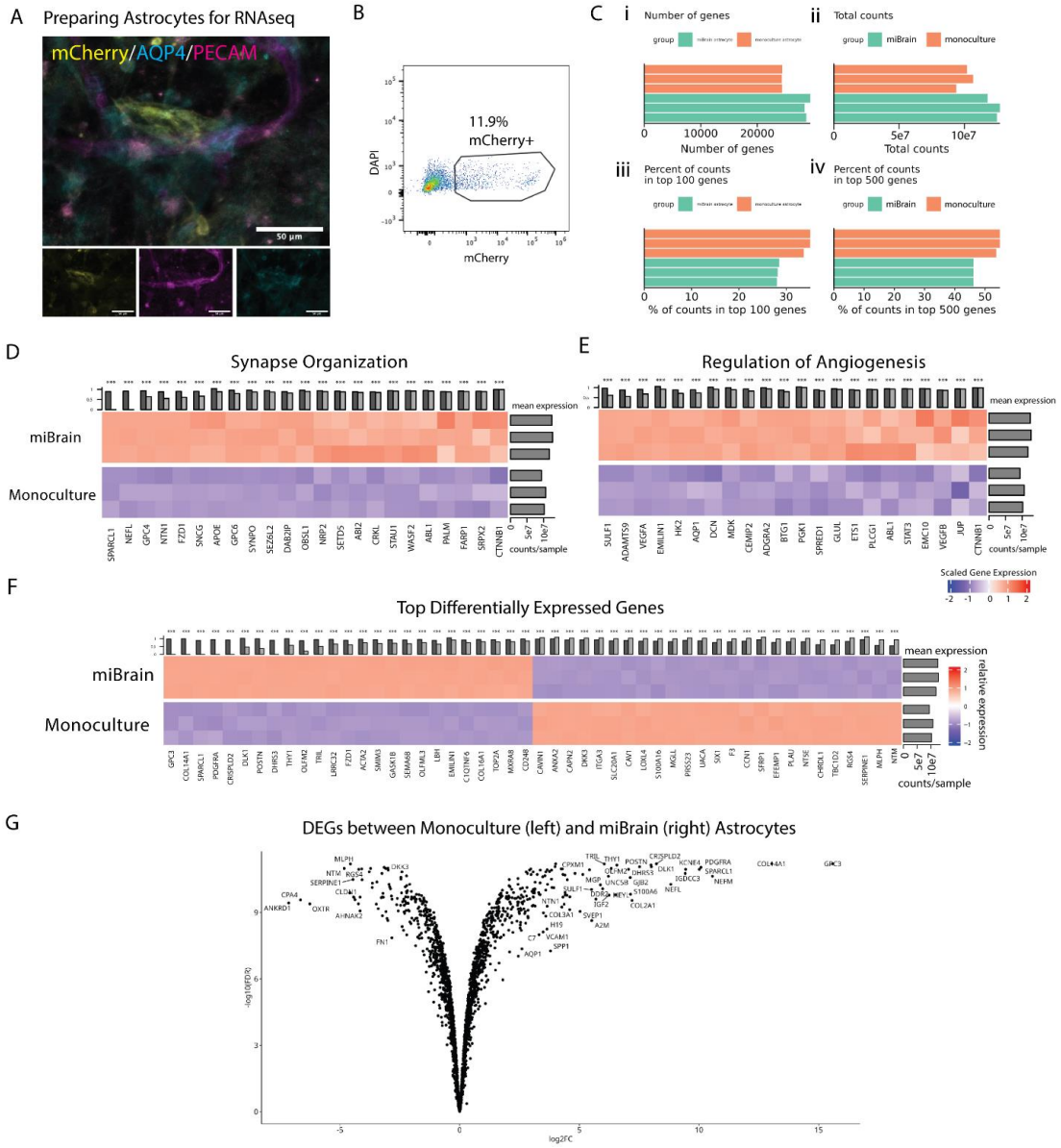

Fig. S4: Transcriptomic Analysis of miBrain-Astrocytes. (**A**) mCherry-astrocytes incorporated into miBrains enabling mCherry-based isolation of astrocytes via flow cytometry (yellow: mCherry, magenta: PECAM, cyan: AQP4; scale bars, 50 µm), (**B**) gating of mCherry-positive cells in flow cytometry (**C**) RNA-sequencing of astrocytes in miBrains and astrocyte monocultures: (**i**) genes per sample, (**ii**) total gene counts, (**iii**) percent of gene counts in the top 100 genes, and (**iv**) percent of gene counts in the top 500 genes, (**D**) upregulation in the miBrain-astrocytes of genes associated with synapse organization (GO:0050808; * $p < 0.05$, ** $p < 0.01$, *** $p < 0.001$), (**E**) upregulation in the miBrain-astrocytes of genes associated with regulation of angiogenesis (GO:0045765; * $p < 0.05$, ** $p < 0.01$, *** $p < 0.001$), (**F**) top DEGs between astrocytes isolated from miBrains versus monocultures sorted by mean expression in miBrain, plotting TMM-normalized and scaled expression (FDR < 0.001), and (**G**) volcano plot displaying these top DEGs between monocultured and miBrain astrocytes (left: upregulated in monocultured astrocytes, right: upregulated in miBrain-astrocytes).

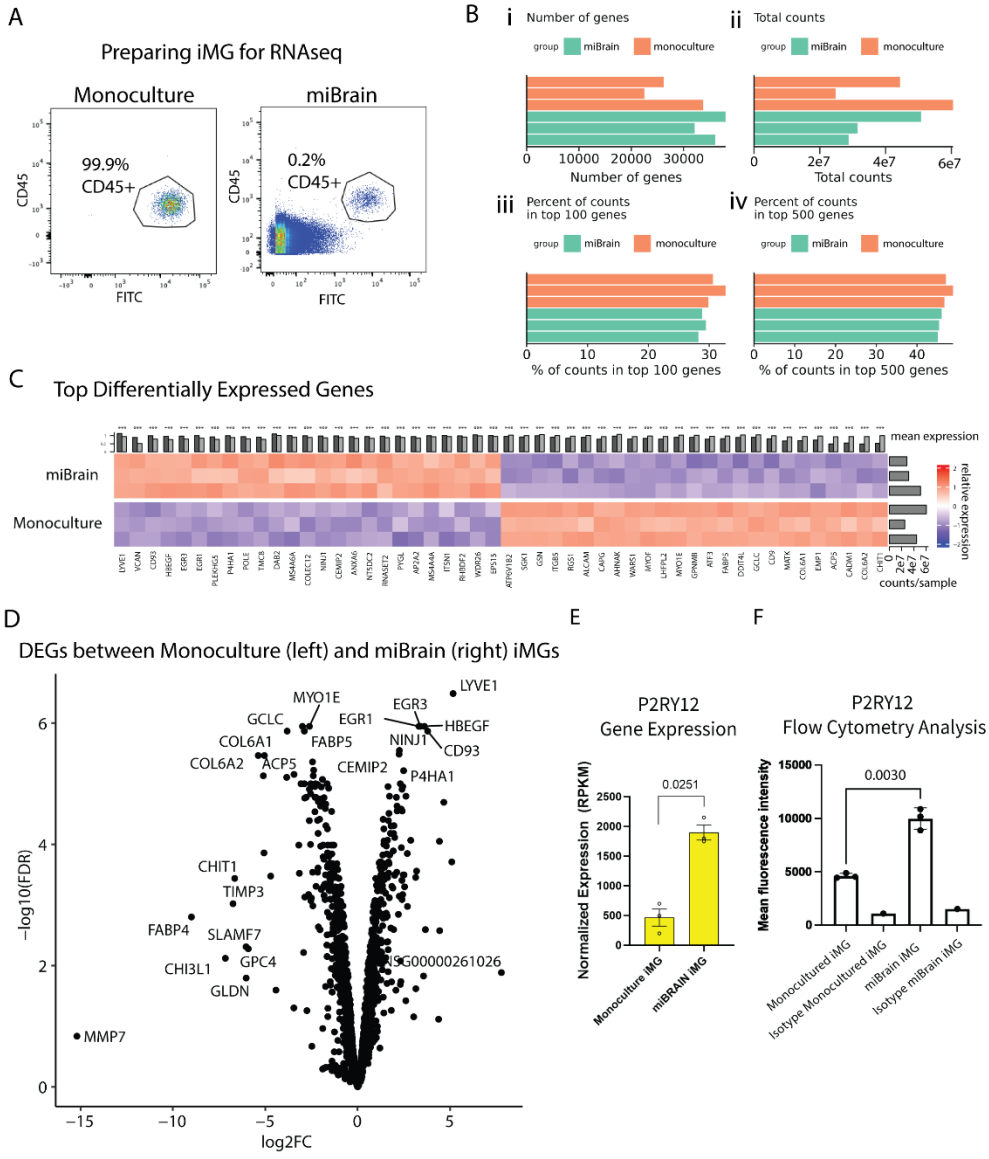

Fig. S5: Transcriptomic Analysis of miBrain-iMG. (**A**) iMG were isolated from miBrains using flow cytometry-based sorting of CD45-positive cells, (**B**) RNA-sequencing of iMG in miBrains and iMG monocultures: (**i**) genes per sample, (**ii**) total gene counts, (**iii**) percent of gene counts in the top 100 genes, and (**iv**) percent of gene counts in the top 500 genes, (**C**) top DEGs between iMG isolated from miBrains versus monocultures sorted by mean expression in miBrain, plotting TMM-normalized and scaled expression (FDR < 0.001), (**D**) volcano plot displaying these top DEGs between monocultured and miBrain iMG (left: upregulated in monocultured iMG, right: upregulated in miBrain-iMG), (**E**) gene expression of *P2RY12* in iMG for monocultures compared to miBrain, and (**F**) validation of P2RY12 differences in iMG between monoculture and miBrain via FACS analysis at the protein level.

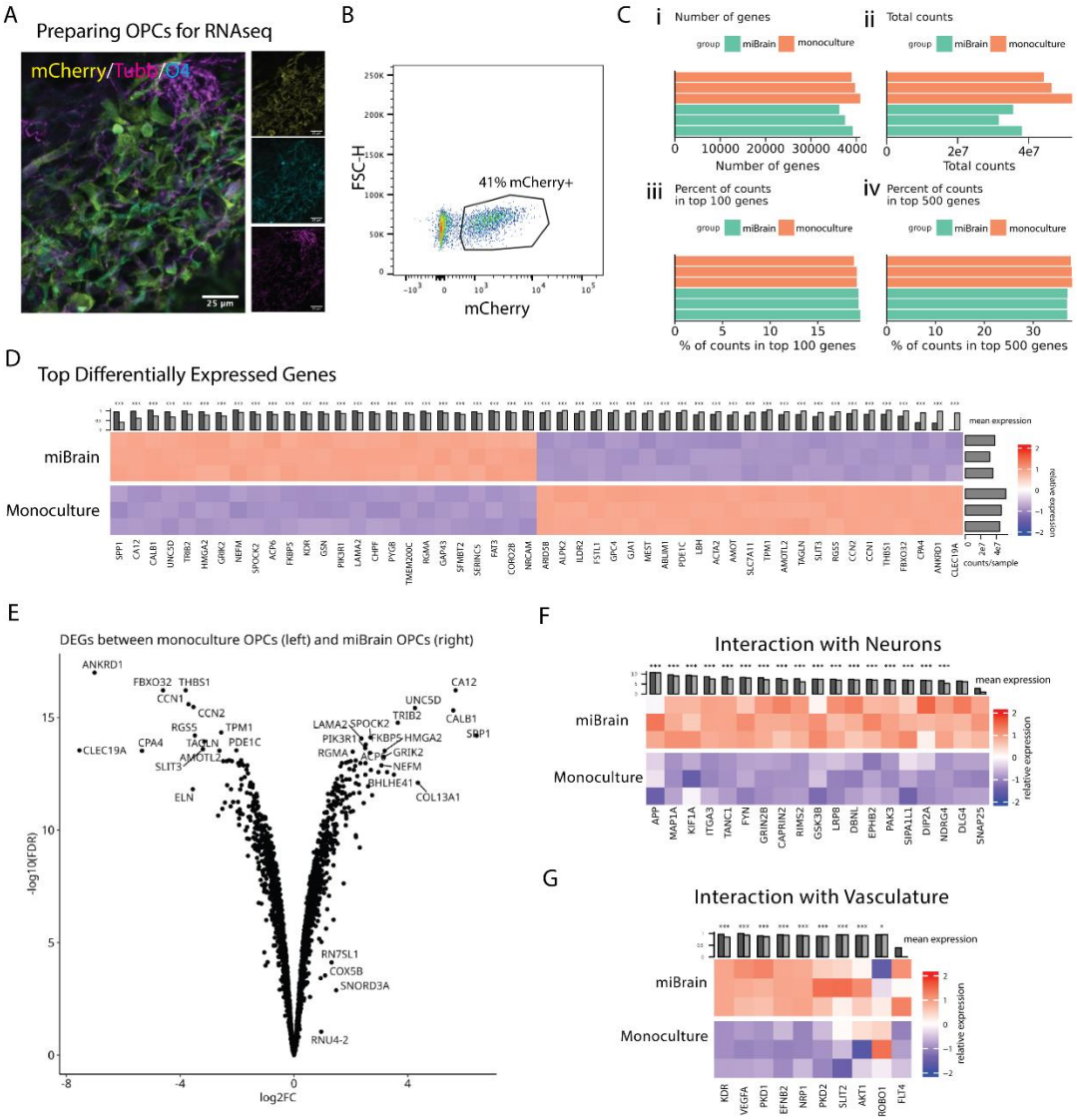

Fig. S6: Transcriptomic Analysis of miBrain-Oligodendroglia. (**A**) mCherry-OPCs incorporated into miBrains enabling mCherry-based isolation of oligodendrocytes via flow cytometry (yellow: mCherry, magenta: TUBB, cyan: O4; scale bars, 25 µm), (**B**) gating of mCherry-positive cells in flow cytometry (**C**) RNA-sequencing of oligodendroglia in miBrains and OPC monocultures: (**i**) genes per sample, (**ii**) total gene counts, (**iii**) percent of gene counts in the top 100 genes, and (**iv**) percent of gene counts in the top 500 genes, (**D**) top DEGs between oligodendrocytes isolated from miBrains versus monocultures sorted by mean expression in miBrain, plotting TMM-normalized and scaled expression (FDR < 0.001), and (**E**) volcano plot displaying these top DEGs between monocultured and miBrain oligodendroglia (left: upregulated in monocultured oligodendroglia, right: upregulated in miBrain-oligodendroglia), (**F**) expression of key *in vivo*-like genes in RNAseq of oligodendroglia isolated from miBrain

compared to monocultured oligodendroglia displayed as TMM-normalized and scaled expression for interactions with neurons and (**G**) interactions with vasculature.

5

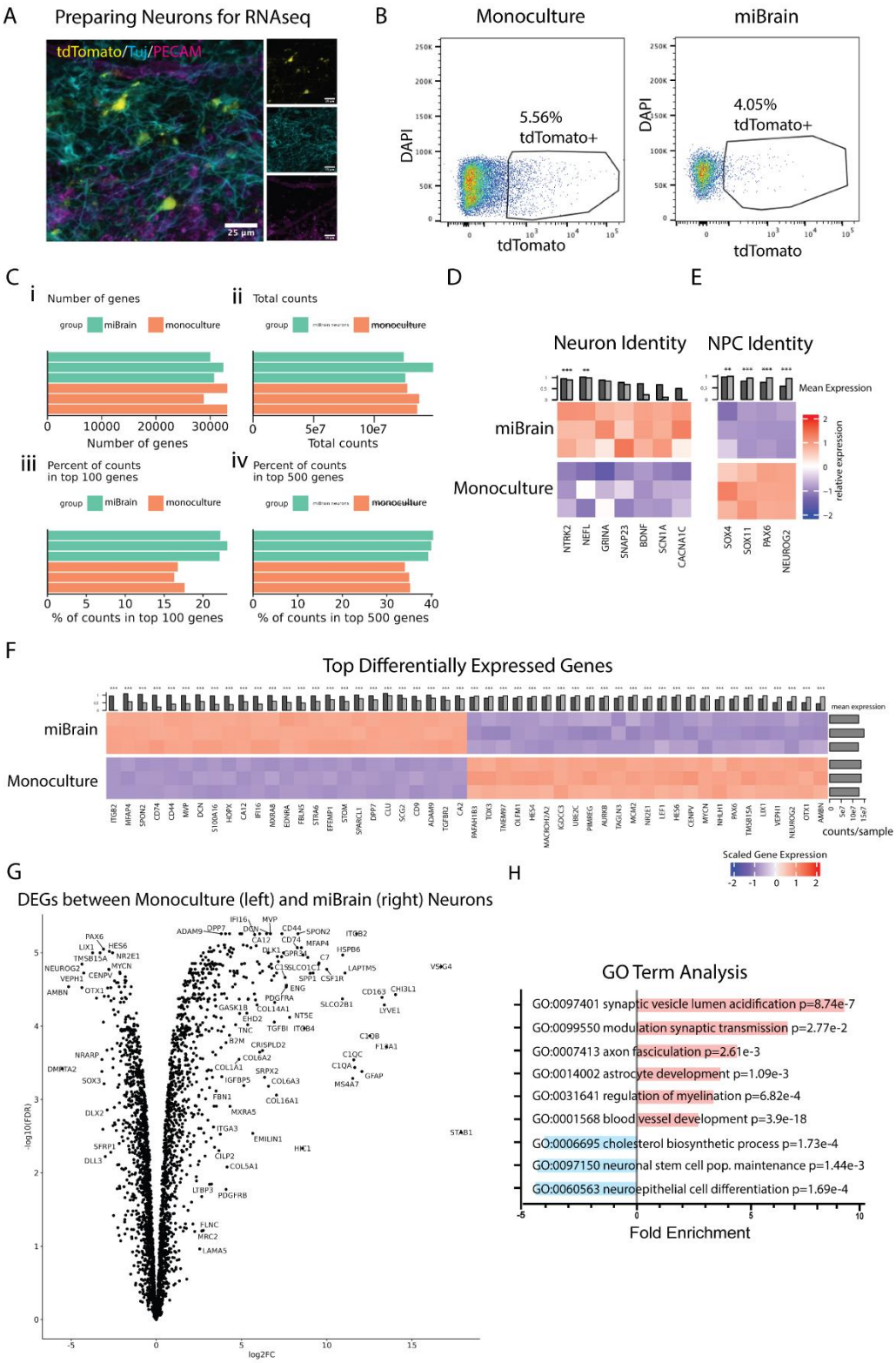

Fig. S7: Transcriptomic Analysis of miBrain-Neurons. (**A**) tdTomato-neurons incorporated into miBrains enabling tdTomato-based isolation of neurons via flow cytometry (yellow: tdTomato, magenta: PECAM, cyan: Tuj; scale bars, 25 µm), (**B**) gating of tdTomato-positive cells in flow cytometry (**C**) RNA-sequencing of neurons in miBrains and neurons monocultures: (**i**) genes per sample, (**ii**) total gene counts, (**iii**) percent of gene counts in the top 100 genes, and

(**iv**) percent of gene counts in the top 500 genes, (**D**) upregulation in the miBrain-neurons of genes associated with neuron identity and (**E**) downregulation upregulation in the miBrain-neurons of genes associated with NPC identity, (**F**) top DEGs between neurons isolated from miBrains versus monocultures sorted by mean expression in miBrain, plotting TMM-normalized and scaled expression (FDR < 0.001), (**G**) volcano plot displaying these top DEGs between monocultured and miBrain neurons (left: upregulated in monocultured neurons, right: upregulated in miBrain- neurons), and (**H**) gene ontology analysis of iMG RNAseq for biological pathways significantly altered in miBrain-cultured iMG based on significantly upregulated and downregulated DEGs and with an FDR p-value less than 0.05.

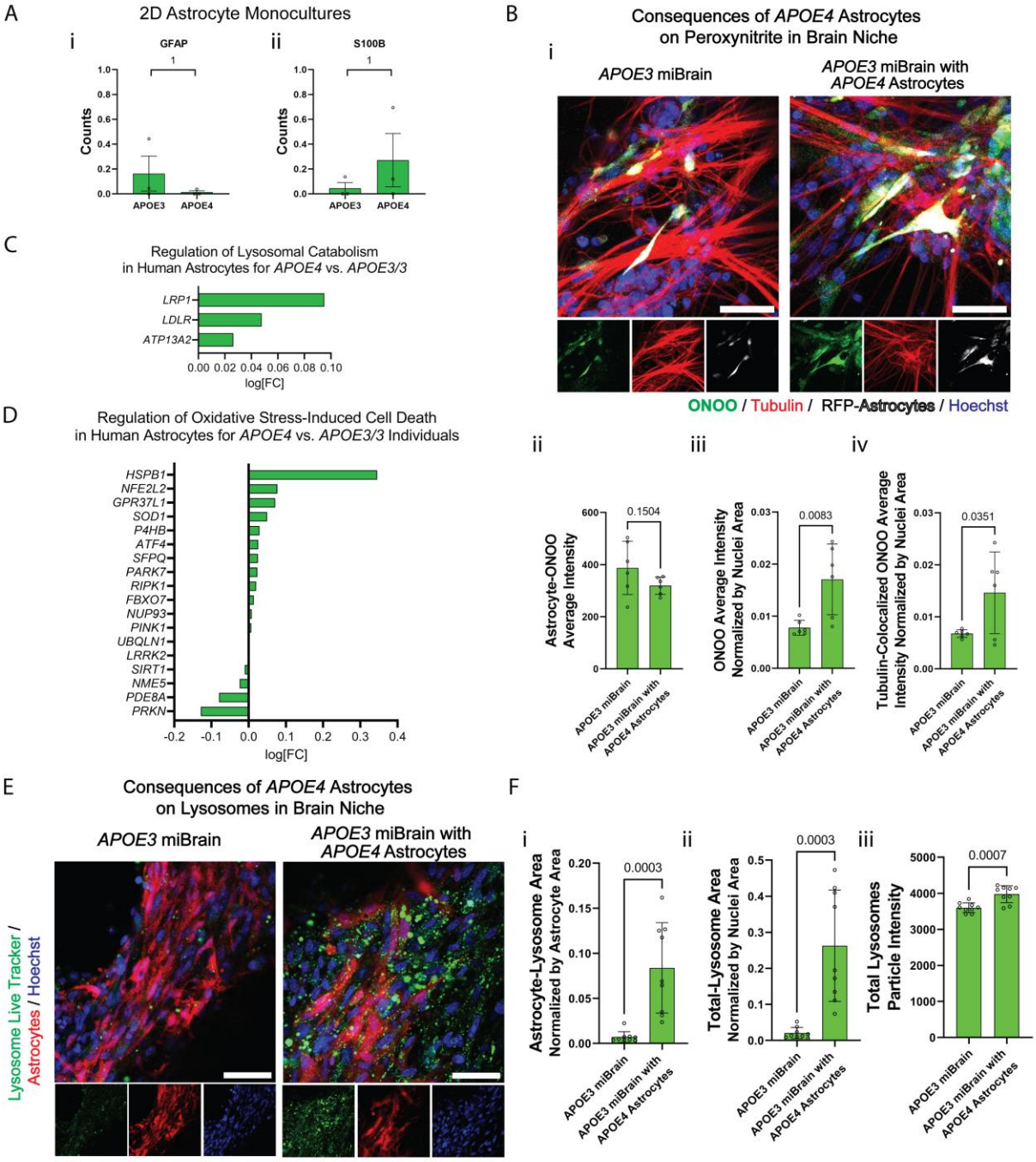

Fig. S8: *APOE4* Astrocyte Dysregulation in miBrain. (**A**) Gene expression counts from 2D astrocyte monocultures from previously published RNA-seq dataset (*48*) for (i) *GFAP* and (ii) S100β, (**B)** Peroxynitrite (ONOO) in miBrains with (i) *APOE3* (left) versus *APOE4* (right) astrocytes incorporated into otherwise-*APOE3* miBrains (green: ONOO, red: live tubulin label, gray: RFP-astrocytes, blue: Hoechst; scale bars, 50 µm), and (ii-iv) quantification of peroxynitrite in terms of (ii) mean intensity of peroxynitrite in astrocyte-colocalized regions, (iii) overall mean intensity of peroxynitrite normalized by nuclei area, and (iv) mean intensity of peroxynitrite in tubulin-colocalized region normalized by nuclei area (data from n = 3 replicates and images from n = 9 max projections from confocal z-stacks; statistical analysis via t test;

experiment was conducted in 3 independent trials), (**C,D**) DEGs in human astrocytes from snRNAseq data set (*17*) in *APOE3/4* and *APOE4/4* versus *APOE3/3* individuals (positive log[FC] is upregulated in *APOE4*) for pathway genes in (**C**) regulation of lysosomal protein catabolic process (GO:1905165) and (**D**) regulation (GO:1903201), positive regulation (GO:1903209), and negative regulation (GO:1903202) of oxidative stress-induced cell death, (**E**) lysosomes in miBrains with *APOE3* (left) versus *APOE4* (right) astrocytes incorporated into otherwise-*APOE3* miBrains (green: lysosome live tracker, red: RFP-astrocytes, blue: Hoechst; scale bars, 50 µm), and (**F**) quantification of lysosomes in terms of (i) area of lysosomes co-localized with astrocytes normalized by astrocyte area, (ii) total segmented lysosome area normalized by nuclei area, and (iii) intensity of segmented lysosome "particles" (data from n = 3 replicates and images from n = 9 fields of view; statistical analysis via t test; experiment was conducted in 3 independent trials).

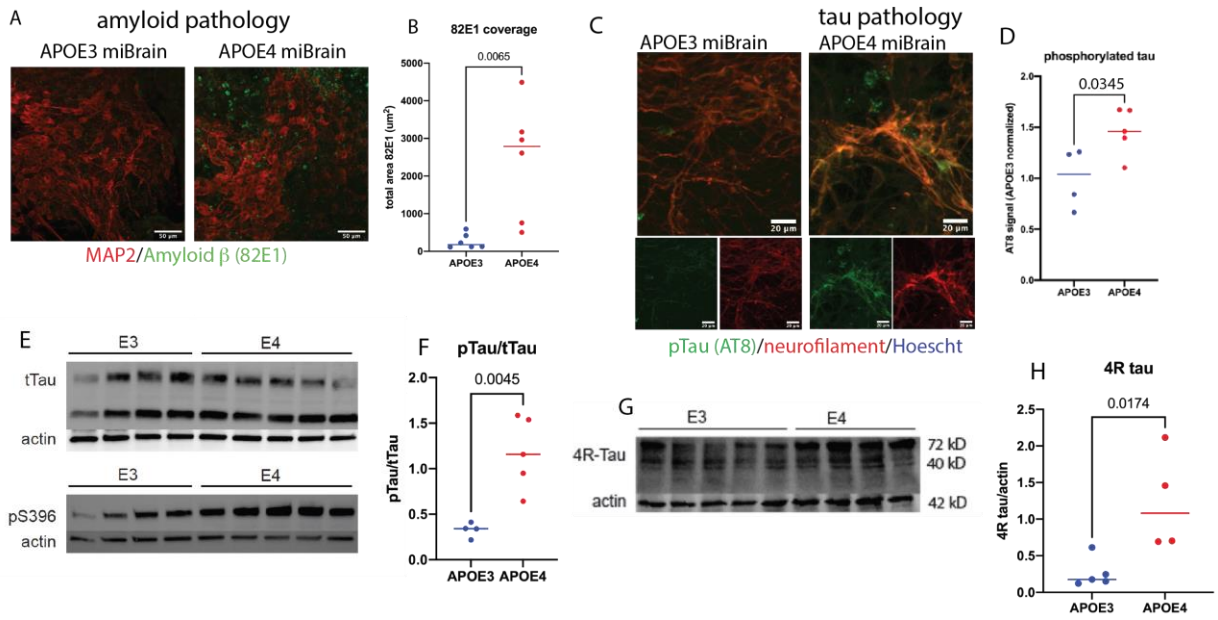

Fig. S9: Endogenous amyloid and tau pathologies in *APOE4* miBrain. (**A**) Amyloid aggregate accumulation in *APOE4* (right) compared to *APOE3* (left) miBrains at week 14 (green: amyloid 82E1, red: MAP2; scale bars, 50 μm), (**B**) quantification of total area of 82E1-positive aggregates normalized to cell density in the field of view (n = 6; student's unpaired t test, p = 0.0065), (**C**) immunoreactivity to hyperphosphorylated tau in neurons in *APOE3* (left) versus *APOE4* miBrains (right) at 14 week (green: AT8, red: neurofilament, blue: Hoechst; scale bars, 50 μm), (**D**) quantification of hyperphosphorylated tau as intensity of AT8 signal co-localized with neurofilament-positive cells, normalized to the *APOE3* condition (n = 4; student's t test, p = 0.034), (**E**) western blot analysis for total tau (tTau) and pS396 for *APOE3* and *APOE4* miBrains, using actin as a housekeeping probe for normalization, (**F**) quantification of pS396 between *APOE3* and *APOE4* miBrains, plotted as pTau normalized by tTau, (**G**) western blot analysis for 4R-Tau for *APOE3* and *APOE4* miBrains, using actin as a housekeeping probe for normalization, and (**H**) quantification of 4R-Tau bands.